

1 **Impact of the Asian Monsoon Anticyclone on the Variability of mid-**  
2 **to-upper tropospheric methane above the Mediterranean Basin**

3  
4 **P. Ricaud<sup>1</sup>, B. Sič<sup>1</sup>, L. El Amraoui<sup>1</sup>, J.-L. Attié<sup>1,2</sup>, R. Zbinden<sup>1</sup>, P. Huszar<sup>3</sup>, S. Szopa<sup>4</sup>, J.**  
5 **Parmentier<sup>1</sup>, N. Jaidan<sup>1</sup>, M. Michou<sup>1</sup>, R. Abida<sup>1</sup>, F. Carminati<sup>1,2,5</sup>, D. Hauglustaine<sup>4,6</sup>, T.**  
6 **August<sup>7</sup>, J. Warner<sup>5</sup>, R. Imasu<sup>8</sup>, N. Saitoh<sup>9</sup> and V.-H. Peuch<sup>10</sup>**

7  
8 <sup>1</sup>CNRM-GAME, Météo-France/CNRS UMR 3589, Toulouse, France

9 <sup>2</sup>Université de Toulouse, Laboratoire d'Aérodynamique, CNRS UMR 5560, Toulouse, France

10 <sup>3</sup>Department of Meteorology and Environment Protection, Faculty of Mathematics and Physics,  
11 Charles University, Prague, V Holešovičkách 2, Prague 8, 18000, Czech Republic

12 <sup>4</sup>Laboratoire des Sciences du Climat et de l'Environnement, CNRS UMR 1572, Gif sur Yvette,  
13 France

14 <sup>5</sup>University of Maryland, College Park, Maryland, USA

15 <sup>6</sup>Laboratoire Image Ville Environnement, CNRS UMR 7362, Strasbourg, France

16 <sup>7</sup>EUMETSAT, Darmstadt, Germany

17 <sup>8</sup>University of Tokyo, Tokyo, Japan

18 <sup>9</sup>Center for Environmental Remote Sensing, Chiba University, Japan

19 <sup>10</sup>European Centre for Medium-Range Weather Forecasts, Reading, UK

20  
21 Correspondence to: P. Ricaud (philippe.ricaud@meteo.fr)

22 In revision, *Atmospheric Chemistry and Physics Discussions*

23 Version 17, 19 September 2014

24

**24 Abstract**

25 The space and time variabilities of methane ( $\text{CH}_4$ ) total column and upper tropospheric mixing  
26 ratios are analyzed above the Mediterranean Basin (MB) as part of the Chemical and Aerosol  
27 Mediterranean Experiment (ChArME<sub>x</sub>) programme. Since the analysis of the mid-to-upper  
28 tropospheric  $\text{CH}_4$  distribution from spaceborne sensors and model outputs is challenging, we have  
29 adopted a climatological approach and have used a wide variety of datasets. We have combined  
30 spaceborne measurements from the Thermal And Near infrared Sensor for carbon Observations-  
31 Fourier Transform Spectrometer (TANSO-FTS) instrument on the Greenhouse gases Observing  
32 SATellite (GOSAT) satellite, the Atmospheric InfraRed Spectrometer (AIRS) on the AURA  
33 platform and the Infrared Atmospheric Sounder Interferometer (IASI) instrument aboard the  
34 MetOp-A platform with model results from the Chemical Transport Model (CTM) MOCAGE, and  
35 the Chemical Climate Models (CCMs) CNRM-AOCCM and LMDz-OR-INCA (according to  
36 different emission scenarios). In order to minimize systematic errors in the spaceborne  
37 measurements, we have only considered maritime pixels over the MB. The period of interest spans  
38 from 2008 to 2011 considering satellite and MOCAGE data and, regarding the CCMs, from 2001 to  
39 2010. Although  $\text{CH}_4$  is a long-lived tracer with lifetime of  $\sim 12$  years and is supposed to be well  
40 mixed in the troposphere, an East-West gradient in  $\text{CH}_4$  is observed and modelled in the mid-to-  
41 upper troposphere with a maximum in the Western MB in all seasons except in summer when  $\text{CH}_4$   
42 accumulates above the Eastern MB. The peak-to-peak amplitude of the East–West seasonal  
43 variation in  $\text{CH}_4$  above the MB in the upper troposphere (300 hPa) is weak but almost twice greater  
44 in the satellite measurements ( $\sim 25$  ppbv) than in the model data ( $\sim 15$  ppbv). The maximum of  $\text{CH}_4$   
45 in summer above the Eastern MB can be explained by a series of dynamical processes only  
46 occurring in summer. The Asian monsoon traps and uplifts high amounts of  $\text{CH}_4$  to the upper  
47 troposphere where they build up. The Asian Monsoon Anticyclone redistributes these elevated  $\text{CH}_4$   
48 amounts towards North Africa and Middle East to finally reach and descent in the Eastern MB. In

49 the lower troposphere, the CH<sub>4</sub> variability is mainly driven by the local sources of emission in the  
50 vicinity of the MB.

51

## 51 **1. Introduction**

52 During the last decades, the impact and the role that atmospheric trace gases play in climate  
53 and air pollution changes have been the source of major concerns. In Intergovernmental Panel on  
54 Climate Change (IPCC, 2007), the ongoing changes of our atmosphere (composition, climate, air  
55 pollution, radiation) are reported. Among trace gases, methane (CH<sub>4</sub>), carbon dioxide (CO<sub>2</sub>), and  
56 nitrous oxide (N<sub>2</sub>O) are predominant constituents which play an important role in atmospheric  
57 changes because they are strongly influenced by human activities. In the frame of predicting the  
58 future of the Earth's climate (IPCC, 2007), knowledge of today's CO<sub>2</sub>, CH<sub>4</sub> and N<sub>2</sub>O sources and  
59 sinks, spatial distribution and time variability is essential and this study will be dedicated to CH<sub>4</sub>.

60 The net positive radiative impact of the human activity on climate, starting from 1750, has been  
61 evaluated to 1.6 [+0.6 to +2.4] Wm<sup>-2</sup> (IPCC, 2007). In the atmosphere, these long-lived greenhouse  
62 gases, e.g., CH<sub>4</sub>, N<sub>2</sub>O and CO<sub>2</sub>, account for 2.63 ± 0.26 Wm<sup>-2</sup> and are the predominant radiative  
63 terms. CO<sub>2</sub>, with tropospheric lifetime of 30–95 years, has a radiative efficiency of 1.4×10<sup>-5</sup> Wm<sup>-2</sup>  
64 ppb<sup>-1</sup>, but CH<sub>4</sub> and N<sub>2</sub>O, with tropospheric lifetimes of 12 and 114 years, respectively, are  
65 intensely more efficient by 3.7×10<sup>-4</sup> and 3.03×10<sup>-3</sup> Wm<sup>-2</sup>ppb<sup>-1</sup>, respectively. IPCC (2007) estimated  
66 CH<sub>4</sub> and N<sub>2</sub>O to be responsible of 0.48 [+0.43 to 0.53] and 0.16 [+0.14 to 0.18] Wm<sup>-2</sup>, respectively  
67 in the radiative forcing changes.

68 The Mediterranean Basin (MB) is located in a transitional zone between subtropical and mid-  
69 latitudes regimes (Lionello, 2012), highly sensitive to climate change. To illustrate, global (or  
70 regional) model simulations tend to show a pronounced decrease in precipitation (2000-2100),  
71 especially in the warm season (Giorgi and Lionello, 2008), and Lionello (2012) reported on an  
72 observed summer West-East asymmetry in precipitation over the MB (1979-2002). In terms of  
73 anthropogenic pollution sources, the MB is at the confluence of three continents, Europe, Africa  
74 and Asia. The impact of these distinct continental sources such as from industrial and densely  
75 populated coastal areas (e.g. Marseille, Barcelona, Athens, Tunis, Cairo, Genoa or Roma)  
76 (Kanakidou et al, 2011; Im and Kanakidou, 2012) or forest fires (e.g. South East of France, Corsica,



77 Portugal, Greece) (Cristofanelli et al., 2013) is still not perfectly understood, especially on the O<sub>3</sub>  
78 and CO budgets in which CH<sub>4</sub> interplays through complex reactions with nitrogen oxides (NO<sub>x</sub>)  
79 (Dentener et al., 2005). Besides these regional sources, polluted air masses may originate from Asia  
80 during the summer monsoon period (Randel and Park, 2006), Africa through the Hadley cell and  
81 upper level anticyclone (Ziv et al., 2004; Liu et al., 2009) and North America through the westerlies  
82 (Christoudias et al., 2012). The Expérience sur Site pour Contraindre les Modèles de Pollution  
83 atmosphérique et de Transport d'Emission (ESCOMPTE) campaign (June-July 2001) aimed to  
84 characterize the summer time pollution events in the vicinity of Marseille, France (Cros et al.,  
85 2004). The goal of the Mediterranean Intensive Oxidant Study (MINOS) campaign (July-August  
86 2001) in the eastern Mediterranean was to measure long-range transport of air pollution and  
87 aerosols from South East Asia and Europe towards the MB (Ladstätter-Weissenmayer et al., 2003;  
88 Scheeren et al., 2003). They have demonstrated the importance of coastal and synoptic transport  
89 mechanisms on the variability of constituents but were not adapted to assess the budgets of O<sub>3</sub>, CO  
90 and long-lived species.

91 The ChArMEx (Chemistry and Aerosol Mediterranean Experiment) Project  
92 (<http://charmex.lsce.ipsl.fr/>) is the atmospheric chemistry component of a large multidisciplinary  
93 Mediterranean regional program proposed and conducted by France. It intends, among other  
94 objectives, to quantify processes explaining the temporal evolution of chemical compounds and  
95 aerosols in the troposphere above the Mediterranean Basin (MB). To achieve these goals over the  
96 first phase (2010-2015), the program uses data from satellites, ground-based, sondes, aircraft,  
97 models and assimilation in order to evaluate 1) the variabilities and recent trends of several species  
98 (e.g. O<sub>3</sub>, CO, N<sub>2</sub>O) and aerosols, 2) the synoptic-scale circulation that controls their transport, and  
99 3) the future chemical climate over the MB by 2100.

100 The past/present nadir-viewing instruments able to actually measure CH<sub>4</sub> in the troposphere have  
101 been/are:

102 1) the Interferometric Monitor for Greenhouse gases (IMG) instrument operating in the Thermal  
103 Infrared (TIR) aboard the ADvanced Earth Observing Satellite (ADEOS-1) platform in 1996-1997  
104 (Clerboux et al., 1998);

105 2) the near-IR (NIR) Scanning Imaging Absorption Spectrometer for Atmospheric Chartography  
106 (SCIAMACHY) aboard the ENVIronment SATellite (ENVISAT) platform (Buchwitz et al., 2000)  
107 from 2002 to 2012;

108 3) the Tropospheric Emission Spectrometer (TES) operating in the TIR aboard the Aura platform  
109 (Worden et al., 2012) from 2004 to date;

110 4) the Thermal And Near infrared Sensor for carbon Observations – Fourier Transform  
111 Spectrometer (TANSO-FTS) on the Greenhouse gases Observing SATellite (GOSAT) platform  
112 (Yokota et al., 2009) both in the Short-Wave InfraRed (SWIR) and in the TIR from 2008 to date;

113 5) the Atmospheric InfraRed Sounder (AIRS) aboard the Aqua platform (Xiong et al., 2008)  
114 measuring in the TIR from 2004 to date;

115 6) the Infrared Atmospheric Sounding Interferometer (IASI) instrument aboard the MetOp-A  
116 and -B platforms (Hilton et al., 2012) operating in the TIR from 2008 to date, and aboard the  
117 MetOp-C platform expected to be launched in 2016.

118 Table 1 synthesizes the above mentioned information and shows the nadir-viewing instrument  
119 capability to measure tropospheric CH<sub>4</sub>. The sensitivity of the TIR to measure CH<sub>4</sub> is rather weak  
120 except on areas showing a high thermal contrast at the surface (vertical gradient of temperature  
121 between the surface and the lowermost planetary boundary layer) as the ones encountered over the  
122 tropics (Crevoisier et al., 2013) contrarily to the measurements performed in the SWIR (Yoshida et  
123 al., 2013). In the NIR, analyses are essentially restricted to areas over land because the retrievals  
124 over sea are considered less reliable due to fairly low surface albedo of water, which results in low  
125 signals and thus in low signal-to-noise ratios (Georgoulias et al., 2011).

126 In parallel to the satellite data, models have also been used in order to assess the variability,  
127 sources and sinks, and future trends of the long-lived species. Examples are: CH<sub>4</sub> emission and flux

128 estimates at global scales (Bergamaschi et al., 2009; Bousquet et al., 2011), future evolution of  
129 long-lived species included in the international Atmospheric Chemistry and Climate Model  
130 Intercomparison Project (ACCMIP) involving more than 10 different models (Lamarque et al.,  
131 2013).

132 Numerous studies have examined the variabilities of atmospheric compounds above the MB to  
133 highlight the processes (sources and sinks) associated by coupling surface, balloon-borne, airborne,  
134 spaceborne measurements with models results at different scales, from mesoscales to global scales.  
135 Constituents are for instance aerosols (Nabat et al., 2012), radionuclides (Masson et al., 2010),  
136 ozone (Liu et al., 2009), carbon monoxide (Drori et al., 2012). From these references, we note the  
137 impact of 1) the different meteorological regimes and 2) the seasonal variabilities of the emissions  
138 of atmospheric constituents, e.g. CO emitted from fires in summers, produces a seasonal variation  
139 in all the constituents. It also produces a longitudinal gradient between the Eastern and the Western  
140 MB, together with a seasonal variation in the gradient. For example, European anthropogenic  
141 emissions were found to significantly influence the Eastern MB surface CO concentrations, while  
142 European biomass burning emissions were found to have only a small impact on Eastern MB  
143 surface CO concentrations (Drori et al., 2012). Total columns of CH<sub>4</sub> as measured by  
144 SCIAMACHY over land and the Eastern Mediterranean from 2003 to 2004 show latitudinal and  
145 seasonal variations that cannot be attributed to volcano eruptions (Georgoulias et al., 2011).

146 The aim of the present paper is to assess the variability of CH<sub>4</sub> in the mid-to-upper troposphere  
147 between the East and the West of the Mediterranean Basin and to attribute the seasonal variability  
148 of the East-West gradient to different processes at both, synoptic and global scales depending on the  
149 season and the altitude layer considered. We will study in detail the impact of the summer-time  
150 long-range transport of CH<sub>4</sub> from Asia to the Eastern MB through the Asian Monsoon Anticyclone.  
151 Since we have already underlined that measurement and modeling of the tropospheric CH<sub>4</sub>  
152 distribution are challenging, we will adopt a climatological approach and will use a wide variety of  
153 space-borne measurements and model outputs to verify that they give consistent results.

154 We have collected the maximum amount of information available from satellite  
155 measurements along with model results in order to study the variability of tropospheric CH<sub>4</sub> over  
156 the MB and to assess the processes driving this variability. We have thus built a wide dataset  
157 combining all these pieces of information keeping in mind that 1) it is out of the scope of the  
158 present paper to perform a validation of satellite products, 2) all these datasets have their own  
159 strengths and weaknesses, and 3) the more data we gather, the better the statistics are and  
160 furthermore, the dataset consistency can be better assessed. Regarding space-borne measurements,  
161 we have considered tropospheric columns of CH<sub>4</sub> from IASI over the period 2008-2011, and upper  
162 tropospheric CH<sub>4</sub> profiles from AIRS and GOSAT over the periods 2008-2011 and March-  
163 November 2010, respectively. Regarding the models, we have considered three types of chemical  
164 models to calculate CH<sub>4</sub> variability in the mid-to-upper troposphere. The MOCAGE (Josse et al.,  
165 2004) chemical transport model (CTM), constrained by the ARPEGE meteorological analyses, is  
166 expected to give CH<sub>4</sub> vertical profiles more realistic than climate models over a specified period.  
167 Nevertheless, the short spin-up period (3 months vs. 12 years of CH<sub>4</sub> lifetime) used in the  
168 MOCAGE runs may impact the CH<sub>4</sub> distribution. On the other hand, chemical climate models  
169 (CCMs) as LMDz-OR-INCA (Hauglustaine et al., 2004; Szopa et al., 2013) from the Laboratoire  
170 des Sciences du Climat et de l'Environnement (LSCE) and CNRM-AOCCM (Huszar et al., 2013)  
171 from Météo-France are run over a much longer period (greater than 10 years) than MOCAGE and  
172 should be better suited to study the climatological variability of CH<sub>4</sub> over the MB. The LMDz-OR-  
173 INCA is mainly dedicated to the tropospheric CH<sub>4</sub> profiles since it takes into account the major  
174 surface processes that can drive the CH<sub>4</sub> variability in the entire troposphere depending on the  
175 inventory scenarios (see section 2.2.3). The CNRM-AOCCM is mainly dedicated to the upper  
176 tropospheric-stratospheric CH<sub>4</sub> profiles because it has a detailed description of the stratosphere and  
177 should better describe the processes impacting the CH<sub>4</sub> variability in the upper troposphere-lower  
178 stratosphere. The 3 models are thus complementary in the study of the CH<sub>4</sub> variability in the mid-  
179 to-upper troposphere over the MB.

180 The manuscript is structured as follow. In section 2, we briefly present the spaceborne  
181 instruments and datasets involved in this study, namely MetOp-A/IASI, AQUA/AIRS and  
182 GOSAT/TANSO together with the models, namely MOCAGE, CNRM-AOCCM and LMDz-OR-  
183 INCA. The meteorology and climatology of CH<sub>4</sub> inferred from the different datasets above the MB  
184 are discussed in section 3. The CH<sub>4</sub> variability both in the East and in the West of the MB is  
185 presented in section 4. A detailed discussion of the different processes involved in the CH<sub>4</sub>  
186 variability above the MB is presented in section 5 underlining the impact of the Asian Monsoon  
187 Anticyclone to the distribution of the mid-to-upper CH<sub>4</sub> in the Eastern MB. Finally, section 6  
188 concludes the paper.

189

## 190 **2. Datasets**

### 191 2.1. Satellite data

192 Our study analyses CH<sub>4</sub> measurements from three different spaceborne TIR sensors (IASI, AIRS  
193 and GOSAT) and consider only the pixels over the Mediterranean Sea due to the larger systematic  
194 biases over land. The sensitivity of TIR retrievals strongly depends on surface parameters:  
195 emissivity, temperature and thermal contrast (Claeyman et al., 2011). The amplitude of diurnal  
196 cycle, and its spatial variability, is larger over land than over the sea. Sea surface temperature  
197 exhibits a diurnal amplitude weaker than land surface temperature. Therefore, the vertical  
198 sensitivity of the TIR measurements, defined as the full-width at half-maximum of the averaging  
199 kernels from the optimal estimation method (Rodgers, 2000), over the sea is consistent during day  
200 and night and concentrated in the mid-troposphere. Over the land, the vertical sensitivity is, on  
201 average, lower in the middle troposphere during the day than during the night, depending on the  
202 actual value of the thermal contrast at the surface.

203 Infrared sounders measurement errors can be rather large, e.g. up to 10% or more for a single  
204 CH<sub>4</sub> total column IASI pixel (Turquety et al., 2004). Thus by applying temporal  
205 (monthly/seasonally) and geographical averages, including more than a thousand measurements, we

206 can lower the random error to less than 1%. Systematic errors, if any, will of course be unchanged.  
207 For that reason, our analysis relies on a differential method to highlight the CH<sub>4</sub> variability by  
208 considering the difference between the Eastern MB (EMB) and the Western MB (WMB), assuming  
209 that the systematic errors are of the same order of magnitude (although partially unknown) within  
210 each geographical box that will be defined in section 3.

211

### 212 *2.1.1. The IASI data*

213 IASI, on board of MetOp-A, was launched in 2006 by the European Organisation for the  
214 Exploitation of Meteorological Satellites (EUMETSAT). More specifications on platform and  
215 instrument can be found on <http://smc.cnes.fr/IASI> and [http://www.eumetsat.int/Home/](http://www.eumetsat.int/Home/Main/Satellites/Metop/Instruments/SP_2010053151047495)  
216 [Main/Satellites/Metop/Instruments/SP\\_2010053151047495](http://www.eumetsat.int/Home/Main/Satellites/Metop/Instruments/SP_2010053151047495)). The retrieval algorithm for CH<sub>4</sub> is  
217 based on the neural network theory adapted from Turquety et al. (2004). The retrieval method is  
218 embedded in the operational IASI Level 2 product processing facility at EUMETSAT  
219 (EUMETSAT, 2004; Schlüssel et al., 2005, August et al., 2012). From the spectral bandwidth  
220 1230-1347 cm<sup>-1</sup>, the estimated accuracy of the CH<sub>4</sub> total column is about 2% and the estimated  
221 precision is of the order of 10% (Turquety et al., 2004). The true accuracy cannot be stated without  
222 reference to independent means of comparison, which are not available so far. Consequently, we  
223 consider a random Gaussian error of ~10% associated with each single pixel of retrieved total  
224 column of CH<sub>4</sub>. At mid-latitudes, the vertical sensitivity of the total column CH<sub>4</sub> is peaking in the  
225 mid-troposphere at ~8 km from 4 to 14 km (Razavi et al., 2009) and, in the tropics, at ~10 km from  
226 5 to 15 km. Geophysical level 2 pre-operational data are provided by EUMETSAT (from version 4  
227 to version 5 from 2008 to 2011). The CH<sub>4</sub> products, not yet validated, are only experimental  
228 products, routinely generated for demonstration and evaluation. Note, the number of daily total  
229 columns of CH<sub>4</sub> averaged in a 1°x1° bin is highly variable because of cloud-free IASI  
230 considerations. The monthly-averaged IASI data within each of the East and West areas defined in  
231 section 3 represent an average of 30000-70000 pixels depending on the month considered.

232

233 *2.1.2. The AIRS data*

234 AIRS is onboard the space platform NASA EOS Aqua, launched in 2002  
235 (<http://airs.jpl.nasa.gov/>). AIRS measures approximately 200 channels in the 7.66  $\mu\text{m}$  absorption  
236 band of  $\text{CH}_4$ , of which 71 channels are used to retrieve  $\text{CH}_4$ . A detailed description of the retrieval  
237 algorithm can be found in Susskind et al. (2011). Note, the averaging kernels provided by NASA  
238 will be considered further (section 4.2) in order to degrade the vertical resolution of the model  
239 outputs. At mid-latitudes, the most sensitive layer of AIRS channels to  $\text{CH}_4$  is at 300 hPa (~9 km)  
240 with a vertical sensitivity from 700 to 100 hPa (Xiong et al., 2008), and, in the tropics, at 200 hPa  
241 from 500 to 70 hPa consistently with the IASI TIR measurement sensitivity. Around 200-300 hPa,  
242 considering the version V5 used in the present analysis (Xiong et al., 2008), the precision of AIRS  
243  $\text{CH}_4$  is estimated to be 30 ppbv (1.7%) and validation using in situ aircraft measurements shows  
244 that the accuracy of the retrieved  $\text{CH}_4$  is 0.5–1.6%. Daily maritime profiles of  $\text{CH}_4$  have been  
245 averaged in  $1^\circ \times 1^\circ$  bins over the MB. The monthly-averaged AIRS data within each of the East and  
246 West areas defined in section 3 represent an average of 6000-10000 vertical profiles depending on  
247 the month considered.

248

249 *2.1.3. The GOSAT data*

250 The Japanese Aerospace Exploration agency (JAXA) launched the GOSAT platform in 2009,  
251 with the TANSO-FTS spectrometer, a nadir-viewing instrument designed for greenhouse gases  
252 research,  $\text{CO}_2$  and  $\text{CH}_4$ , operating in the TIR and SWIR domains [0.7-14.3  $\mu\text{m}$ ] (Kuze et al., 2009).  
253 More specifications on platform and instrument can be found on <http://www.gosat.nies.go.jp/>. The  
254 sensitivity of the SWIR  $\text{CH}_4$  measurements at 1.67  $\mu\text{m}$  (Yokota et al., 2009) at mid-latitudes over  
255 the sea is very weak, thus few meaningful pixels could have been retrieved preventing the use of  
256 such information in our analysis. The TIR measurements from Band 4 (5.5–4.3  $\mu\text{m}$ ) provide  
257 vertical profiles of  $\text{CH}_4$  along 7 vertical levels (Imasu et al., 2007) by using the optimal estimation

258 method with a vertical sensitivity in the tropics peaking at 10 km (higher than at mid-latitudes) from  
259 5 to 15 km (Saitoh et al., 2012), consistently with the vertical sensitivity of IASI (Razavi et al.,  
260 2009) and AIRS (Xiong et al., 2008) in the tropics. A selection by using Degree of Freedom of  
261 Signal (DFS) is applied for the data having DFS values larger than 0.6 for CH<sub>4</sub>. TIR data (L2  
262 Version 0.10) were only available from 16 March to 24 November 2010 from the GOSAT User  
263 Interface Gateway at the time the analysis has been performed. These retrievals provide vertical  
264 profiles of mixing ratio of CH<sub>4</sub> from 1000 to 100 hPa. Comparisons with aircraft measurements  
265 show that the average difference between the GOSAT (TIR) and aircraft CH<sub>4</sub> values (TIR –  
266 aircraft) is –5 ppbv, and the 1 $\sigma$  standard deviation is 15 ppbv (Saitoh et al., 2012). Daily maritime  
267 profiles of CH<sub>4</sub> have been averaged in 1°x1° bins over the MB. The monthly-averaged GOSAT data  
268 within each of the East and West areas defined in section 3 represent an average of 100-300 vertical  
269 profiles depending on the month considered, namely 20-30 times less than for AIRS.

270

## 271 2.2. The model data

### 272 2.2.1. The MOCAGE data

273 MOCAGE (MODèle de Chimie Atmosphérique à Grande Echelle) (Peuch et al., 1999) is a 3D  
274 CTM which covers the planetary boundary layer, the free troposphere, and the stratosphere for  
275 different applications such as: operational chemical weather forecasting (Dufour et al., 2005);  
276 tropospheric and stratospheric research studies (Claeyman et al., 2010; Ricaud et al., 2009); and  
277 data assimilation research (El Amraoui et al., 2010; Claeyman et al., 2011). In our study, MOCAGE  
278 is forced dynamically by wind and temperature fields from the analyses of the ARPEGE model  
279 (Courtier et al., 1991). The MOCAGE horizontal resolution is 2°x2° and the model uses a semi-  
280 Lagrangian transport scheme. It includes 47 levels from the surface up to 5 hPa with a vertical  
281 resolution of about 800 m around the tropopause, 400-800 m in the troposphere and 40-400 m in the  
282 7 levels of the boundary layer. Chemistry used within MOCAGE is a combination of tropospheric  
283 (RACM described in Stockwell et al., 1997) and stratospheric (REPROBUS described in Lefèvre et



284 al., 1994) chemical schemes. Initial chemical conditions are taken from climatological fields over a  
285 spin-up period of 3 months allowing the model to quickly bring chemical fields to realistic spatial  
286 distributions. Surface emissions prescribed in MOCAGE are based upon yearly- or monthly-  
287 averaged climatologies. More precisely, the CH<sub>4</sub> surface emissions are monthly averages and split  
288 into anthropogenic sources taken from the Intergovernmental Panel on Climate Change (IPCC)  
289 (Dentener et al., 2005), biomass burning (van de Werf et al., 2003) and biogenic sources (Michou  
290 and Peuch, 2002). The CH<sub>4</sub> climatologies are representative of year 2000 for a total emission rate of  
291 534 Tg(CH<sub>4</sub>) yr<sup>-1</sup>.

292

### 293 2.2.2. *The CNRM-AOCCM data*

294 The atmospheric model embedded in CNRM-AOCCM is presented in Huszar et al. (2013)  
295 based on the Atmosphere-Ocean General Circulation Model (AOGCM) CNRM-CM5 described in  
296 Voltaire et al. (2012). The main difference between CNRM-CM5 and CNRM-AOCCM resides in  
297 the “online” coupling with a stratospheric chemistry which is based on the REPROBUS scheme.  
298 This scheme is applied on the whole vertical column, except between the surface and the 560 hPa  
299 level where long-lived chemical species are relaxed towards global average surface value following  
300 the A1B scenario from IPCC (2007). The A1B scenario mainly describes a future world of very  
301 rapid economic growth, global population that peaks in mid-century and declines thereafter, and the  
302 rapid introduction of new and more efficient technologies. Convection of species is not considered.  
303 In this chemistry version, the 3-D distribution of the seven absorbing gases (H<sub>2</sub>O, CO<sub>2</sub>, O<sub>3</sub>, CH<sub>4</sub>,  
304 N<sub>2</sub>O, CFC11, and CFC12) is then provided by the chemistry module of CNRM-AOCCM and  
305 interacts with the radiative calculations. More details can be found in Michou et al. (2011). In the  
306 present version, there are about 50 chemical species, and the horizontal resolution is 2.8°x2.8°.  
307 Distribution of atmospheric constituents at the surface are zonally symmetric below 500 hPa (Fig.  
308 10) and greenhouse gases follow the A1B scenario on atmospheric chemistry and climate for the

309 period of 1940-2100. In the present analysis, for this model, we only consider the climatological  
310 period 2001-2010.

311

### 312 *2.2.3. The LMDz-OR-INCA data*

313 The INteraction between Chemistry and Aerosol (INCA) model is used to simulate the  
314 distribution of aerosols and gaseous reactive species in the troposphere. In the present  
315 configuration, the model includes 19 hybrid vertical levels extending up to 4 hPa, and a horizontal  
316 resolution of 1.9° in latitude and 3.75° in longitude. INCA is coupled online to the LMDz General  
317 Circulation Model (GCM) to account, with different degrees of complexity, for climate chemistry  
318 interactions. In the simulations described here, LMDz is coupled with the ORCHIDEE (Organizing  
319 Carbon and Hydrology in Dynamic Ecosystems) dynamic global vegetation model (Krinner et al.,  
320 2005) for soil/atmosphere exchanges of water and energy (Hourdin et al., 2006), but not for  
321 biogenic CO<sub>2</sub> or Volatile Organic Compounds (VOCs) fluxes. Together, these three models form  
322 the LMDz-OR-INCA model. Fundamentals for the gas phase chemistry are presented in  
323 Hauglustaine et al. (2004) and first results with the full tropospheric gaseous chemical scheme are  
324 presented by Folberth et al. (2006). The model includes 223 homogeneous chemical reactions, 43  
325 photolytic reactions and 6 heterogeneous reactions including non-methane hydrocarbon oxidation  
326 pathways and aerosol formation. The LMDz-OR-INCA simulation covers four future projections of  
327 emissions for the 2000–2100 period. The Representative Concentration Pathways (RCP) emissions  
328 are used (Lamarque et al., 2011). They correspond to emission trajectories compatible with the  
329 evolution of radiative forcing equivalent in 2100 to 2.6, 4.5, 6.0 and 8.5 Wm<sup>-2</sup> relative to pre-  
330 industrial values (labelled therein after RCP 2.6, 4.5, 6.0 and 8.5). In the present analysis, for this  
331 model, we only consider the climatological period 2001-2010.

332

333

334

### 335 **3. Atmospheric conditions controlling the spatial distribution of methane**

336 Figure 1 shows the CH<sub>4</sub> fields calculated by MOCAGE for summer (June-July-August, JJA)  
337 2009 over the MB at 850, 500 and 200 hPa, superimposed with the wind fields from the ARPEGE  
338 analyses averaged over the same period. Figure 2 presents the CH<sub>4</sub> vertical distribution as  
339 calculated by MOCAGE in summer 2009 along an East-West axis above the MB. Similarly to  
340 Figures 1-2, the Figures 3-4 present, in winter (December-January-February, DJF) 2009, the CH<sub>4</sub>  
341 fields as calculated by MOCAGE over the MB at 850, 500 and 200 hPa, and along an East-West  
342 axis, respectively. On Figures 2 and 4, the MOCAGE CH<sub>4</sub> fields are superimposed with 1) the wind  
343 fields from ARPEGE analyses and 2) the cold point tropopause pressure fields provided by the  
344 National Centers for Environmental Prediction (NCEP)/National Center for Atmospheric Research  
345 (NCAR) reanalyses, all these data being averaged over the same period.

346 Considering the meteorology of the MB, we observe two different regimes. 1) In winter (Fig. 3),  
347 and more generally from autumn to spring (not shown), from the boundary layer to the upper  
348 troposphere, air masses are essentially coming from either Europe or Eastern Atlantic Ocean. 2) In  
349 summer (Fig. 1), the meteorology of EMB and WMB is more complex and depends on the altitude  
350 considered.

351 In the planetary boundary layer in summer (Fig. 1, bottom), cells develop in the WMB, and air  
352 masses come from Europe, Northern Africa and Eastern Atlantic Ocean, whilst in the EMB, air  
353 masses are originated from four major source regions: i) long fetch of maritime European air  
354 masses from NW throughout the whole year, ii) North east continental flow originating in south  
355 Eastern Europe (Etesian winds) in summer, iii) South-east flow from the Arabian Peninsula  
356 occurring in the fall, and iv) South-west flow along the North-African coast most frequent during  
357 late winter and spring (Dayan, 1986). In the middle troposphere (Figs. 1 and 3, middle), whatever  
358 the season, air masses are essentially coming from the west for both parts of the basin. In summer  
359 (Fig. 1, top), upper tropospheric air masses in the WMB are essentially coming from the West, but  
360 in the EMB, they are also originated from Northern Africa and the Arabic Peninsula (Ziv et al.,

361 2004; Liu et al., 2009), and even farther away, from Asia (we will discuss this point in sections 4  
362 and 5). Note that, in summer, the EMB and WMB are also affected by the location of the  
363 descending branch of the Hadley cell (Fig. 2). These summer climatologies are all consistent with  
364 Millán et al. (1997), Lelieveld et al. (2002), Ziv et al. (2004) and Schicker et al. (2010).

365 Seasonally-averaged wind fields from ARPEGE analyses show two different regimes in the  
366 surface pressure values during the summer (Fig. 1, bottom) and the winter (Fig. 3, bottom) periods.  
367 During the summer in the WMB, there is a higher pressure regime than in the EMB (Fig. 1,  
368 bottom). In the lowermost troposphere (850 hPa), an anticyclonic cell develops in the WMB that  
369 has an impact on the distribution of CH<sub>4</sub> by producing a local minimum (Fig. 1, bottom). At 850  
370 hPa, air masses are coming from Europe, North Africa and the Atlantic Ocean. The CH<sub>4</sub>  
371 distribution shows a maximum over Europe, consistently with the strongest emission zones (Fig.  
372 10), and a strong minimum over North Africa. In the mid-troposphere (500 hPa), air masses are  
373 coming from Europe, and the Atlantic Ocean (Fig. 1, middle). An East-West gradient is detected  
374 with more CH<sub>4</sub> on the EMB. In the upper troposphere (200 hPa) (Fig. 1, top), air masses are  
375 originated from the Atlantic Ocean (even North America) and from North Africa and Asia  
376 producing over the MB an obvious North-South gradient with more CH<sub>4</sub> in the South (upper  
377 troposphere) than in the North (lower stratosphere) attributed to the impact of long-range transport  
378 of pollutants (as discussed in section 5). A systematic subsidence is present over the MB (Fig. 2)  
379 whatever the longitudinal bin considered due to the presence of semi-permanent subtropical high  
380 pressure systems which are centred over the tropical deserts. More precisely, in the WMB, the  
381 descent is caused by the presence of a high pressure cell (Fig. 1, bottom) whilst, in the EMB, it is  
382 coming from the Hadley cell that is further displaced over the Northern Africa producing a  
383 downward branch in the area 30°N-35°N. The tropopause moves up from ~200 hPa in the WMB to  
384 ~175 hPa in the EMB (Fig. 2). The CH<sub>4</sub> distribution shows 1) an obvious transition at the  
385 tropopause and 2) a minimum in the West and a maximum in the East in the low troposphere

386 accentuated by the systematic descent in the Eastern MB that brings CH<sub>4</sub>-enriched air masses from  
387 the upper troposphere to the mid-to-low troposphere.

388 In winter, the meteorological condition of the MB is much more homogeneous with westerlies  
389 blowing whatever the pressure considered from 850 to 200 hPa (Figs. 3-4). North-South (and to a  
390 lesser extent East-West) gradients in CH<sub>4</sub> can also be detected (Fig. 3) associated to the local  
391 sources of emission over Europe at 850 hPa and to the stratosphere/troposphere transition at 200  
392 hPa. The 500-hPa layer is a transition region between the low and the upper troposphere with  
393 minima of CH<sub>4</sub> over North Africa and a cell of high CH<sub>4</sub> in the WMB (Fig. 3, middle). Contrarily to  
394 summer, since the temperature of the Mediterranean Sea is greater than that of the surrounding  
395 continents, a systematic upward motion is present (Fig. 4) whatever the longitudinal bin considered.  
396 The Hadley cell is further displaced to the South (latitude < 30°N) and its downward branch does  
397 not affect significantly the EMB. The tropopause pressure is rather stable from the WMB to the  
398 EMB, around 260 hPa. The CH<sub>4</sub> distribution shows minimum in the lowermost troposphere and a  
399 maximum in the middle troposphere (Fig. 4).

400

## 401 **4. CH<sub>4</sub> variability**

### 402 *4.1. CH<sub>4</sub> spatial distribution of the MB*

403 Figure 5 shows the distributions of 1) the CH<sub>4</sub> total columns from IASI over the MB averaged in  
404 summer 2009 to compare with the MOCAGE results in time coincidence, and 2) the CH<sub>4</sub> mixing  
405 ratios from AIRS at 260 hPa over the MB averaged in summer 2009 to compare with the  
406 MOCAGE results at 200 hPa in time coincidence. The measured and modelled data are selected  
407 only for the maritime pixels within the boxes [36°N-45°N, 1°E-12°E] and [30°N-37°N, 26°E-37°E]  
408 to represent the WMB and the EMB (blue squares in each figure), respectively.

409 Due to its long lifetime (~12 years), CH<sub>4</sub> is considered as a well-mixed species in the  
410 troposphere. Nevertheless the CH<sub>4</sub> spatial distribution over the MB in summer (JJA) 2009 shows  
411 some gradients both in the East-West and the North-South directions. Indeed, in the middle

412 troposphere (inferred from the sensitivity of the IASI total columns) and in the upper troposphere  
413 (200-260 hPa), an East-West gradient is observed in the model and satellite data of ~60 ppbv (~4%)  
414 in total column and ~30-150 ppbv (~2-9%) in mixing ratio. A North-South gradient is also detected  
415 in the MOCAGE and AIRS data but not in the IASI data set. Therefore, there is systematically a  
416 maximum of CH<sub>4</sub> from the middle to the upper troposphere in the East of the MB compared to the  
417 West. In the mid-to-upper troposphere, these East-West gradients are not originated from the CH<sub>4</sub>  
418 sources more intense in Europe than in Northern Africa or in Middle Asia (Fig. 1) but rather from  
419 the long-range transport of Asian-origin air masses and the subsidence of air masses in the EMB  
420 (Figs. 1-2 and detailed discussion in section 5).

421 Quantitatively, there is a positive bias in MOCAGE vs. IASI of less than 30 ppbv (2%) in CH<sub>4</sub>  
422 total column mixing ratio. The East-West gradient is consistent between IASI and MOCAGE but  
423 the North-South modelled gradient is not detected in the IASI data set. In the upper troposphere  
424 (200-260 hPa), MOCAGE and AIRS CH<sub>4</sub> mixing ratios are very consistent with gradients more  
425 accentuated in the model (~150 ppbv) than in the AIRS data sets (~30 ppbv). A systematic negative  
426 bias of MOCAGE compared to AIRS of ~100 ppbv up to 150 ppbv (10%) in the Northern MB is  
427 detected. We discuss in the next section the consistency of the vertical profiles of CH<sub>4</sub> measured by  
428 the different spaceborne sensors and calculated by MOCAGE together with the associated biases.

429

#### 430 *4.2. Vertical profiles*

431 Figure 6 shows the vertical profiles of CH<sub>4</sub> as measured by AIRS (750-100 hPa) and GOSAT  
432 (1000-100 hPa) and as calculated by MOCAGE (1000-100 hPa) averaged over the EMB and the  
433 WMB depending on the four seasons: winter (DJF), spring (March-April-May, MAM), summer  
434 (JJA) and autumn (September-October-November, SON) 2010. There is a good agreement to within  
435 20-30 ppbv between AIRS and GOSAT data in the vertical domain 750-200 hPa. GOSAT is  
436 systematically greater than AIRS by about 20-30 ppbv for pressure greater than 300 hPa, whilst, for  
437 pressure less than 300 hPa, AIRS is systematically greater than GOSAT by 20 ppbv degrading to

438 50-200 ppbv at 100 hPa. But the shape of the vertical spaceborne profiles is consistent between  
439 AIRS and GOSAT. Separately, whatever the season considered, the MOCAGE low-to-mid  
440 tropospheric CH<sub>4</sub> is low biased compared to the measured profiles by ~150-200 ppbv. Furthermore,  
441 the MOCAGE vertical profiles systematically show a maximum at 300 hPa, that is not present in  
442 any of the spaceborne measurements, and a strong decrease above.

443 In order to assess the impact of the vertical sensitivity of the spaceborne measurements to the  
444 CH<sub>4</sub> profiles, we have applied the AIRS averaging kernels, derived from the AIRS retrieval method  
445 (Susskind et al., 2011) and provided by NASA for each AIRS pixel, to the profiles calculated by  
446 MOCAGE. Note that the AIRS a priori vertical profiles are not used in our study since we are only  
447 interested in the vertical shape of the CH<sub>4</sub> profile and not the absolute amount of CH<sub>4</sub>. Degrading  
448 the vertical resolution of the MOCAGE profiles by the convolution of averaging kernels (Fig. 6)  
449 does show a strong impact on the vertical shape of the CH<sub>4</sub> profiles since the strong maximum at  
450 300 hPa is no longer present. Convolved MOCAGE CH<sub>4</sub> profiles are now consistent with AIRS  
451 CH<sub>4</sub> profiles whatever the season considered but a systematic low bias of ~150-200 ppbv (8-10%)  
452 between AIRS and MOCAGE convolved profiles is observed. This might be due to the fact that no  
453 a priori information contributes to the convolved profile. This is also due to the overall  
454 underestimation of CH<sub>4</sub> by global models. Indeed, due to coarse horizontal resolution and large  
455 uncertainties in the estimated surface emissions, tropospheric CH<sub>4</sub> lifetimes, e.g. evaluated by the  
456 multi-model intercomparison project ACCMIP, are about 5-13% lower than observation estimates  
457 (Naik et al., 2013; Voulgarakis et al., 2013).

458 Along the vertical, it is almost impossible to validate the spaceborne profiles with an external  
459 data set since, even within the Total Carbon Column Observing Network  
460 (<http://www.tccon.caltech.edu/>) giving accurate and precise column-averaged abundances of CH<sub>4</sub>  
461 (Wunch et al., 2010) because no measurement sites are unfortunately available in the vicinity of the  
462 MB. Near the surface, the amount of CH<sub>4</sub> is about 1700-1750 ppbv for MOCAGE, and is on  
463 average less than the CH<sub>4</sub> GOSAT data by about 150-200 ppbv. At this stage, it is worthwhile

464 considering surface data within the MB. The NOAA Earth System Research Laboratory (ESRL) In  
465 Situ Methane Measurements provide some surface CH<sub>4</sub> measurements within and/or in the vicinity  
466 of the MB: Lampedusa, Italy (35.52°N, 12.62°E, 45 amsl), Centro de Investigacion de la Baja  
467 Atmosfera (CIBA), Spain (41.81°N, 4.93°W, 845 amsl) and Negev Desert, Israel (30.86°N,  
468 34.78°E, 477 amsl). On average, these three sites indicate (not shown) a surface CH<sub>4</sub> annual mean  
469 of about 1 875 ppbv in 2010, with an annual oscillation of ~20 ppbv amplitude. Consequently, the  
470 amount of surface CH<sub>4</sub> in the MOCAGE run for 2010 is actually low biased by about 150-200 ppbv  
471 (8-10%) but is very consistent with the LMDz-OR-INCA surface data of ~1725-1750 ppbv over the  
472 Mediterranean (Fig. 10). The slight differences between the EMB and the WMB according to the  
473 season and height are studied in detail in the next sub-section.

474

#### 475 *4.3. The East-West seasonal variations: measured and calculated differences*

476 The seasonal variations of the differences in CH<sub>4</sub> fields between the EMB and the WMB (i.e.,  
477 EMB minus WMB, labelled as “E–W”) as measured by AIRS, GOSAT and IASI and as calculated  
478 by LMDz-OR-INCA, CNRM-AOCCM and MOCAGE are presented in Figure 7 when considering  
479 the upper troposphere (AIRS, GOSAT, LMDz-OR-INCA and CNRM-AOCCM at 260 and 300  
480 hPa) and the middle troposphere (IASI and MOCAGE total column mixing ratios). In the middle  
481 and upper troposphere (Fig. 7), despite the fact that spaceborne measurements and modelling of  
482 CH<sub>4</sub> are challenging, the modelled and measured seasonal variations of E–W are consistent to each  
483 other showing a maximum (peak) in summer and a wide minimum in winter.

484 If we consider the time evolution of the total column mixing ratios (namely focussing on the  
485 middle troposphere), we note that both MOCAGE and IASI show a maximum in summer, although  
486 3 times greater in MOCAGE (~60 ppbv) than in IASI (~20 ppbv) in July and August. The  
487 minimum in January-February is close to zero but slightly positive in October (5-10 ppbv). The  
488 much stronger maximum in August calculated by MOCAGE compared to IASI CH<sub>4</sub> total columns  
489 might be attributable to the sensitivity of spaceborne measurements in the middle troposphere



490 whilst the MOCAGE tropospheric columns cover the entire troposphere from the surface to the top  
491 of the model atmosphere, namely 5 hPa.

492 In the upper troposphere (300 hPa), the spaceborne instrument datasets show a E–W maximum  
493 in summer of ~12 ppbv in August for AIRS and a E–W wide maximum of ~5 ppbv in July-  
494 September for GOSAT. A E–W peak of ~10 ppbv in July-August is also calculated by CNRM-  
495 AOCCM although, in the LMDz-OR-INCA dataset, the E–W maximum is slightly positive in  
496 August (~2 ppbv). The minimum in the satellite datasets is observed in March-April and is negative  
497 (from –15 to –20 ppbv) consistently with the LMDz-OR-INCA dataset whilst the CNRM-AOCCM  
498 E–W minimum is less intense (–6 ppbv in February and April). The peak-to-peak amplitude of the  
499 E–W seasonal variation is almost twice greater in the satellite measurements (~25 ppbv) than in the  
500 model data (~15 ppbv). This represents a ~1.5-2.0% variation of CH<sub>4</sub> in the E–W over the entire  
501 year. These results suggest that the difference in amplitude between satellite and model in the  
502 seasonal evolution of E-W may be due to: a) the comparison technique, the vertical resolution of the  
503 models is much better than the vertical resolution of the satellite observations; b) regarding the  
504 processes in summer, we may have less CH<sub>4</sub> trapped in the Asian Monsoon Anticyclone  
505 redistributed towards the EMB (see section 5) in the models compared to the measurements; c)  
506 regarding the processes in winter, since westerlies are mainly present over the MB in the mid-to-  
507 upper troposphere (Figs. 3 and 8), we may have too much and/or too rapidly CH<sub>4</sub> transported over  
508 the Mediterranean Sea to the East compared to the West, leading to a too smooth E-W gradient in  
509 the models compared to the measurements.

510 We have also to remind that statistically the number of spaceborne measurements used in our  
511 analysis (see section 2) is ~5 times greater in IASI compared to AIRS, ~30 times greater in AIRS  
512 compared to GOSAT. Consequently, GOSAT monthly-averaged data appear noisier than AIRS  
513 monthly-averaged data. Note that IASI total columns are not and cannot be directly compared with  
514 AIRS or GOSAT profiles in our analysis. Nevertheless, although IASI data are not operationally  
515 produced, the IASI E-W seasonal variation is very consistent with the E-W seasonal variation as

516 deduced from all other datasets. The monthly random error attributed to the E–W IASI CH<sub>4</sub> is about  
517 0.1%, much less than the observed peak-to-peak yearly variation. We estimate that the AIRS  
518 monthly random error attributed to the E–W CH<sub>4</sub> is twice greater than the one calculated for IASI,  
519 and that the GOSAT monthly random error is about 5 times greater than the ones calculated for  
520 IASI. We discuss in the next section the origin of the summer peak in the E–W seasonal variation.

521

## 522 **5. Contribution of the Asian Monsoon Anticyclone**

523 As stated in sections 3 and 4, interpreting the E–W CH<sub>4</sub> seasonal variation along the vertical  
524 requires to consider the distribution of CH<sub>4</sub> over the Asian continent because of the importance of  
525 long-range transport. From Rodwell and Hoskins (1996), it is known that there is a meteorological  
526 link between monsoons and the dynamics of the deserts and more precisely between the Asian  
527 monsoon and the EMB summer regime. The subsidence centre over the EMB owes its location,  
528 timing of onset and intensity to the Asian monsoon, and not to the Hadley circulation. Although it  
529 takes less than one day to reach the upper troposphere within the Asian monsoon, back-trajectory  
530 calculation (Ziv et al., 2004) shows that it takes about 3-4 days for an air parcel to reach and descent  
531 the upper tropospheric EMB from the vicinity of the anticyclone that develops over the Asian  
532 monsoon. Inside the Asian Monsoon Anticyclone (AMA), pollutants like CO originating from the  
533 surface constitute about 50% of the CO concentration at 100 hPa (Park et al., 2009), with the  
534 reminder resulting from chemical production in the troposphere. Most of the CO within the AMA  
535 comes from India and South East Asia, with an insignificant contribution from the Tibetan Plateau.  
536 Randel and Park (2006), and Park et al. (2009) have analyzed in detail this phenomenon over Asia  
537 by considering dynamical parameters (potential vorticity) and chemical species (H<sub>2</sub>O, CO and O<sub>3</sub>).

538 Numerous studies have already evaluated the impact of transport vs. emission of pollutants and  
539 aerosols over the MB and its temporal variability considering different pollutants, chemical  
540 compounds and aerosols (Wanger et al., 2000; Lelieveld et al., 2002; Pfister et al., 2004; Kallos et

541 al., 2007). As stated in section 3, two main dynamic factors affect the EMB: 1) the upper to mid-  
542 tropospheric subsidence, and 2) the lower-level cool Etesian winds (Ziv et al., 2004). Although the  
543 EMB is characterized by strong descent in the middle and upper troposphere in summer, transport  
544 from the boundary layer accounts for about 25% of the local Middle Eastern contribution to the  
545 ozone enhancement in the middle troposphere (Liu et al., 2009). Elevated CO episodes in EMB  
546 during summer can also be attributed to synoptic conditions prone to favorable transport from  
547 Turkey and Eastern Europe towards the EMB rather than increased emissions (Drori et al., 2012).  
548 Upper tropospheric longitudinal gradients in the EMB of CH<sub>4</sub>, CO, hydrocarbons, including  
549 acetone, methanol, and acetonitrile, halocarbons, O<sub>3</sub> and total reactive nitrogen (NO<sub>y</sub>) were also  
550 attributed in August 2001 to the chemical impact of the Asian plume (Scheeren et al., 2003).  
551 Finally, Georgoulias et al. (2011) present some interesting results of CH<sub>4</sub> from space in the vicinity  
552 of the Mediterranean Sea, but only over land and essentially over the Eastern Mediterranean. The  
553 authors found, from the total columns of CH<sub>4</sub> as measured by SCIAMACHY in 2003 and 2004, an  
554 obvious maximum in August that could not be attributed to any volcano eruptions although this  
555 area hosts a significant number of geological formations that could potentially contribute to the total  
556 CH<sub>4</sub> burden. Being given that the sensitivity of the SCIAMACHY CH<sub>4</sub> total columns covers the  
557 vertical domain 1000-200 hPa from the vertical structure of the averaging kernels presented in  
558 Buchwitz et al. (2005), we note that 1) this maximum localized in August is consistent with our  
559 study, and 2) the impact of the AMA on the CH<sub>4</sub> fields in the mid-to-upper troposphere cannot be  
560 ruled out.

561 In order to analyze the climatological impact of the AMA onto the EMB, we have calculated (Fig.  
562 8) the climatological six-day back-trajectories from the point at 33° N, 35° E located in the EMB  
563 (red filled circle on Fig. 8) based on the British Atmospheric Data Centre (BADC) trajectory service  
564 (<http://badc.nerc.ac.uk/community/trajectory/>) from 1st July to 31st August (summer convective  
565 period) from 2001 to 2010 every 12 hours at 5 different pressure levels: 850 and 700 hPa (lower  
566 troposphere), 500 hPa (middle troposphere), and 300 and 200 hPa (upper troposphere). The BADC

567 trajectories were derived from 40-year (ERA40) re-analysis ( $2.5^\circ \times 2.5^\circ$ /pressure levels) produced by  
568 the European Centre for Medium-Range Weather Forecasts (ECMWF). The position of the gravity  
569 centre of each distribution (i.e. the maximum in the probability distribution function) at each level is  
570 represented every 24 hours by a star on Figure 8. This methodology has been firstly used over the  
571 Dome C (Concordia) station in Antarctica (Ricaud, 2014). We have also performed the same  
572 analysis but for the winter period from 1<sup>st</sup> January to 31<sup>st</sup> March 2001-2010 (Fig. 8). Figure 8  
573 undoubtedly shows that air parcels above the EMB during the Asian monsoon period of July-  
574 August from 2001 to 2010 are originated: a) from Asia in the upper troposphere, b) from Northern  
575 America and Northern Africa in the mid-troposphere and c) from Europe in the low troposphere.  
576 The same Figure also shows that in winter (and all other seasons but summer, not shown) air parcels  
577 above the EMB are originated from the West (Europe, Atlantic Ocean, North America, Pacific  
578 Ocean) whatever the pressure level considered from 850 to 100 hPa.

579 We apply the same climatological approach based on the CNRM-AOCCM and LMDz-OR-  
580 INCA CH<sub>4</sub> model results over the period 2001-2010. We consider (Fig. 9) the E–W CH<sub>4</sub> seasonal  
581 evolution at pressure levels from the lowermost troposphere to the lowermost stratosphere (850,  
582 700, 500, 300, 200 and 100 hPa) and different scenarios for LMDz-OR-INCA (RCPs 2.6, 4.5, 6.0  
583 and 8.5) in order to check out whether the summer peak still persists. We also represent the fields of  
584 CH<sub>4</sub> as specified and/or calculated in the lowermost level (surface level) by CNRM-AOCCM and  
585 by LMDz-OR-INCA (4 scenarios) in summer averaged over the climatological period 2001-2010  
586 over a wide area covering the MB and the Asian continent in Figure 10, whilst the CH<sub>4</sub> fields  
587 calculated at 200 hPa are shown in Figure 11.

588 The E-W CH<sub>4</sub> seasonal variations from the two models (Fig. 9) behave distinctively in the entire  
589 troposphere, and agree very well in the lowermost stratosphere. In the lower troposphere (850 and  
590 700 hPa), the E–W CH<sub>4</sub> seasonal evolution from LMDz-OR-INCA exhibits a strong semi-annual  
591 oscillation of  $\pm 10$ -15 ppbv peaking in winter and summer for the 4 RCPs whilst the evolution from  
592 the CNRM-AOCCM shows a weak annual oscillation of 4-5 ppbv amplitude, with a strong

593 minimum in summer, namely out-of-phase relative to the LMDz-OR-INCA variation. In the middle  
594 troposphere at 500 hPa, the 4 LMDz-OR-INCA outputs exhibit a net maximum in August of ~8  
595 ppbv with minima ranging from -2 to -12 ppbv from October to June, whilst the output from  
596 CNRM-AOCCM again shows a strong minimum in summer of about -4 ppbv. At this stage, it is  
597 important to remind that the two models are Global Circulation Models (GCMs) with an on-line  
598 chemistry. The emissions of CH<sub>4</sub> are time-, longitude- and latitude-dependent in LMDz-OR-INCA  
599 with surface maxima over the Northern continent (Fig. 10). In CNRM-AOCCM, there is no  
600 emission of CH<sub>4</sub> (Fig. 10) but mixing ratios of CH<sub>4</sub> between the surface and the 560 hPa level are  
601 relaxed towards evolving global mean surface abundances. This explains why the two models  
602 behave separately for pressures greater or equal to 500 hPa. Note that, regarding the shape of the  
603 E-W CH<sub>4</sub> seasonal evolution, there is no significant difference within the different scenarios of the  
604 LMDz-OR-INCA outputs since surface CH<sub>4</sub> show the same structures independently of the RCPs  
605 considered (Fig. 10).

606 In the upper troposphere (200 and 300 hPa), the outputs from the two models show a peak in  
607 summer in the E-W CH<sub>4</sub> seasonal evolution (Fig. 9), but this differs from the RCPs considered for  
608 LMDz-OR-INCA. The maximum is much more intense in CNRM-AOCCM (~8 ppbv in July-  
609 August and ~30 ppbv in June-July at 300 and 200 hPa, respectively) than in LMDz-OR-INCA (~1  
610 and ~10 ppbv in August for RCP 4.5 but only -4 and +4 ppbv in August for RCP 8.5 at 300 and  
611 200 hPa, respectively; one peak at -4 ppbv in August for RCP 6.0 at 300 hPa but no peak at 200  
612 hPa; no peak for RCP 2.6 neither at 300 nor at 200 hPa). On average, from 500 to 200 hPa, only the  
613 RCP 4.5 scenario from LMDz-OR-INCA shows a positive maximum in summer. At 300 and 200  
614 hPa, the LMDz-OR-INCA summer peak is much less intense than the CNRM-AOCCM summer  
615 peak.

616 It is not obvious to understand why the E-W seasonal variation at 200 hPa is positive in summer  
617 for RCP 4.5 and not for the other RCPs (except RCP 8.5 in August). The horizontal distribution of  
618 CH<sub>4</sub> calculated by the two models at 200 hPa (Fig. 11) drastically differs but local maxima are

619 centred within the AMA. A zonally-symmetric structure showing a strong South-North gradient in  
620 CH<sub>4</sub> is modelled by CNRM-AOCCM with maxima in the tropics (1800 ppbv) and minima at high  
621 latitudes (1700 ppbv) and a local maximum centred within the core of the AMA with values greater  
622 than 1807 ppbv elongated towards two axis: 1) South-East Asia and 2) Middle East and EMB. The  
623 CH<sub>4</sub> field calculated by LMDz-OR-INCA considering the 4 scenarios also shows two maxima over  
624 Northern India and over North-East Asia but the horizontal distribution is not zonally-symmetric  
625 due to a zonally-asymmetric CH<sub>4</sub> surface field. In all the scenarios considered, the CH<sub>4</sub> maxima  
626 within the AMA range from 1710 to 1750 ppbv with increasing RCPs from 2.6 to 8.5. An elongated  
627 tongue of enriched CH<sub>4</sub> enters the EMB. More precisely, we can argue that in RCPs 2.6, 6.0 and  
628 8.5, the primary maximum of CH<sub>4</sub> is located northward at 50°N, 135°E (CH<sub>4</sub> values greater than  
629 1720, 1730 and 1750 ppbv, respectively) although it is a secondary maximum in RCP 4.5 (CH<sub>4</sub>  
630 values less than 1720 ppbv). Through long-range transport, this mid-latitude maximum is  
631 transported Eastward within a band 40°N-50°N enriching CH<sub>4</sub> in the WMB and producing a E-W  
632 minimum in summer for RCPs 2.6, 6.0 and 8.5. Since there is a North-South gradient with a  
633 maximum in the South for CNRM-AOCCM, CH<sub>4</sub>-depleted air masses reach the WMB although  
634 CH<sub>4</sub>-enriched air masses from the AMA reach the EMB producing a systematic peak in summer,  
635 consistently with RCP 4.5.

636 In the lower stratosphere (100 hPa, Fig. 9), all the model outputs are consistent with each other  
637 showing an annual oscillation, with a wide maximum in summer (60-80 ppbv) and a wide minimum  
638 in winter (20-35 ppbv). This is apparently surprising keeping in mind that both models significantly  
639 differ from the surface (see Fig. 10) to ~500 hPa. But, in the WMB, the 100-hPa pressure  
640 corresponds to 420-K potential temperature both in summer (Fig. 2) and in winter (Fig. 4) whilst, in  
641 the EMB, it corresponds to 390 K in summer and 400 K in winter, namely closer to the tropopause  
642 in summer than in winter. Consequently, whatever the model considered, the E-W CH<sub>4</sub> seasonal  
643 variation at 100 hPa a) is always positive and b) shows a peak in the summer period. We note that  
644 the summer peak in E-W seasonal evolution from the middle to the upper troposphere has also been

645 observed and calculated by considering other constituents like CO and O<sub>3</sub> (not shown). This is the  
646 main topic of a forthcoming paper.

647 In conclusion, a schematic representation of the summertime processes impacting mid-to-upper  
648 CH<sub>4</sub> in the EMB is presented in Figure 12. In our study, whatever the amount of CH<sub>4</sub> at the surface  
649 and its horizontal distribution, 1850-2000 ppbv for LMDz-OR-INCA consistently with the emission  
650 sources (Asia, Northern and Eastern Europe, Central Africa) or 1820 ppbv uniformly spread (Fig.  
651 10), the Asian monsoon traps elevated amounts of CH<sub>4</sub> that converge through the depression, and  
652 are uplifted up to the upper troposphere at 200 hPa (Fig. 11) where they build up. At this level, the  
653 AMA re-distributes elevated amounts of CH<sub>4</sub> towards Middle East, North Africa and the EMB  
654 through long-range transport. Finally, elevated amounts of CH<sub>4</sub> build up in the EMB where they  
655 descend to the middle troposphere.

656

## 657 **6. Conclusions**

658 The present study is part of the Chemical and Aerosol Mediterranean Experiment (ChArMEX)  
659 programme. The aim is to investigate the tropospheric CH<sub>4</sub> time and space variations above the  
660 Mediterranean Basin (MB) and to attribute the variability to differing synoptic and global scales  
661 depending on the season and the altitude layer considered. Since the analysis of the mid-to-upper  
662 tropospheric CH<sub>4</sub> distribution from spaceborne sensors and model outputs is challenging, we have  
663 used a wide variety of datasets. 1) The spaceborne measurements from Thermal Infrared (TIR)  
664 instruments: Thermal And Near infrared Sensor for carbon Observations - Fourier Transform  
665 Spectrometer (TANSO-FTS) instrument on the Greenhouse gases Observing SATellite (GOSAT)  
666 satellite, the Atmospheric InfraRed Spectrometer (AIRS) on the Aura platform and the Infrared  
667 Atmospheric Sounder Interferometer (IASI) instrument aboard the MetOp-A platform. 2) The  
668 model results from the Chemical Transport Model (CTM) MOCAGE, and the two Chemical  
669 Climate Models (CCMs) CNRM-AOCCM and LMDz-OR-INCA (the later considering different  
670 emission scenarios, RCPs 2.6, 4.5, 6.0 and 8.5).

671 Since CH<sub>4</sub> is a long-lived tracer with lifetime of ~12 years and is supposed to be well mixed in  
672 the troposphere, we had to adopt a climatological approach to highlight the weak expected  
673 variability. Spaceborne measurements and the model results were selected and monthly-averaged  
674 only over the Mediterranean Sea. The period under interest spans from 2008 to 2011 for the satellite  
675 measurements and the MOCAGE model results whilst, regarding the CCMs, we have averaged the  
676 model outputs over the climatological period from 2001 to 2010.

677 From both satellite and model results, our study obviously demonstrates the persistence of an  
678 East-West gradient in CH<sub>4</sub> from the middle to the upper troposphere with a maximum in the  
679 Western MB whatever the season considered except in summer when larger amounts of CH<sub>4</sub>  
680 accumulate above the Eastern MB. In winter, air masses mainly originating from Atlantic Ocean  
681 and Europe tend to favour an elevated amount of mid-to-upper tropospheric CH<sub>4</sub> in the West  
682 compared to the East of the MB, with a general upward transport above the MB. In summer, the  
683 meteorological condition of the MB is changed, favouring air from Northern Africa and Middle  
684 East together with Atlantic Ocean and Europe, with a general descent above the Eastern MB.

685 Our analysis shows that, in the upper troposphere (300 hPa), the peak-to-peak amplitude of the  
686 East–West seasonal variation in CH<sub>4</sub> above the MB is weak but almost twice greater in the satellite  
687 measurements (~25 ppbv) than in the model data (~15 ppbv).. The maximum of CH<sub>4</sub> in summer  
688 above the Eastern MB can be explained by a series of dynamical processes only occurring in  
689 summer. The Asian monsoon traps and uplifts high amounts of CH<sub>4</sub> to the upper troposphere where  
690 they build up. The Asia monsoon Anticyclone redistributes these elevated CH<sub>4</sub> amounts towards  
691 North Africa and Middle East to finally reach and descent in the Eastern MB. Consequently, the  
692 seasonal variation of the difference in CH<sub>4</sub> between the East and the West MB shows a maximum in  
693 summer for pressures from 500 to 100 hPa considering both spaceborne measurements and model  
694 results whatever the emission scenarios used for the CCMs. But only the RCP 4.5 scenario gives  
695 systematically a positive summer peak whatever the pressure level considered, consistently with the  
696 measurements.



697 From this study, we conclude that CH<sub>4</sub> in the mid-to-upper troposphere over the MB is mainly  
698 affected by long-range transport, particularly intense in summer from Asia. Conversely, in the  
699 lower troposphere, the CH<sub>4</sub> variability is driven by the local sources of emission in the vicinity of  
700 the MB. Other constituents can also be affected by this summer mechanism e.g. O<sub>3</sub> and CO (not  
701 shown). In a forthcoming paper, the time evolution of the CH<sub>4</sub>, O<sub>3</sub> and CO fields above the MB and  
702 at the Asian scale is being studied by considering the outputs from different CCMs in the  
703 contemporary period (2000-2010) in order to study the future evolution of the chemical climate  
704 over the MB by 2100. Finally, despite the fact that IASI CH<sub>4</sub> data as delivered by EUMETSAT are  
705 not operational, the seasonal variation of the East-West difference in CH<sub>4</sub> total columns is  
706 nevertheless consistent with theoretical results and measurements from AIRS and IASI.

707

708 **Acknowledgments.** We would like to thank the following institutes and programme for funding our  
709 study: Centre National de la Recherche Scientifique-Institut National des Sciences de  
710 l'Univers/CNRS-INSU, Centre National des Etudes Spatiales/CNES, Agence de l'Environnement et  
711 de la Maîtrise de l'Energie/ADEME through the programme the Mediterranean Integrated Studies  
712 at Regional And Local Scales/MISTRALS Chemistry-Aerosol Mediterranean  
713 Experiment/ChArMEx. We also thank the following data bases for accessing the data: the French  
714 database Ether, the European Organisation for the Exploitation of Meteorological Satellites, the  
715 GOSAT User Interface Gateway, the National Oceanic and Atmospheric Administration, the British  
716 Atmospheric Data Centre to access the LMDz-OR-INCA model data through the international  
717 Atmospheric Chemistry and Climate Model Intercomparison Project initiative, and the Global  
718 Atmosphere Watch from the World Meteorological Organization. Thanks to the British  
719 Atmospheric Data Centre, which is part of the Natural Environment Research Council (NERC)  
720 National Centre for Atmospheric Science (NCAS), for the calculation of trajectories and access to  
721 European Centre for Medium-Range Weather Forecasts (ECMWF) data. We finally would like to  
722 thank the two anonymous reviewers for their fruitful comments.

723

723 **References**

- 724 August, T., Klaes, D., Schlüssel, P., Hultberg, T., Crapeau, M., Arriaga, A., O'Carroll, A., Coppens,  
725 D., Munro, R., and Calbet, X.: IASI on Metop-A: Operational Level 2 retrievals after five years  
726 in orbit, *J. Quant. Spectrosc. Rad. Transfer*, 113:11, 1340-1371, 2012.
- 727 Bergamaschi, P., Frankenberg, C., Fokke Meirink, J., Krol, M., Villani, M. G., Houweling, S.,  
728 Dentener, F., Dlugokencky, E. J., Miller, J. B., Gatti, L. V., Engel, A., and Levin, I.: Inverse  
729 modeling of global and regional CH<sub>4</sub> emissions using SCIAMACHY satellite retrievals, *J.*  
730 *Geophys. Res.*, 114, D22301, doi:10.1029/2009JD012287, 2009.
- 731 Bousquet, P., Ringeval, B., Pison, I., Dlugokencky, E. J., Brunke, E.-G., Carouge, C., Chevallier,  
732 F., Fortems-Cheiney, A., Frankenberg, C., Hauglustaine, D. A., Krummel, P. B., Langenfelds, R.  
733 L., Ramonet, M., Schmidt, M., Steele, L. P., Szopa, S., Yver, C., Viovy, N., and Ciais, P.: Source  
734 attribution of the changes in atmospheric methane for 2006–2008, *Atmos. Chem. Phys.*, 11,  
735 3689-3700, doi:10.5194/acp-11-3689-2011, 2011.
- 736 Buchwitz, M., Rozanov, V. V., and Burrows, J. P.: A near-infrared optimized DOAS method for  
737 the fast global retrieval of atmospheric CH<sub>4</sub>, CO, CO<sub>2</sub>, H<sub>2</sub>O, and N<sub>2</sub>O total column amounts  
738 from SCIAMACHY Envisat-1 nadir radiances, *J. Geophys. Res.*, 105(D12), 15231–15245,  
739 doi:10.1029/2000JD900191, 2000.
- 740 Buchwitz, M., de Beek, R., Burrows, J. P., Bovensmann, H., Warneke, T., Notholt, J., Meirink, J.  
741 F., Goede, A. P. H., Bergamaschi, P., Körner, S., Heimann, M., and Schulz, A.: Atmospheric  
742 methane and carbon dioxide from SCIAMACHY satellite data: initial comparison with  
743 chemistry and transport models, *Atmos. Chem. Phys.*, 5, 941-962, doi:10.5194/acp-5-941-2005,  
744 2005.
- 745 Cristofanelli, P., Fierli, F., Marinoni, A., Calzolari, F., Duchi, R., Burkhardt, J., Stohl, A., Maione,  
746 M., Arduini, J., and Bonasoni, P.: Influence of biomass burning and anthropogenic emissions on  
747 ozone, carbon monoxide and black carbon at the Mt. Cimone GAW-WMO global station (Italy,  
748 2165 m asl), *Atmos. Chem. Phys.*, 13, 15-30, doi:10.5194/acp-13-15-2013, 2013.

- 749 Christoudias, T., Pozzer, A., and Lelieveld, J.: Influence of the North Atlantic Oscillation on air  
750 pollution transport. *Atmos. Chem. Phys.*, 12, 869-877, doi:10.5194/acp-12-869-2012, 2012.
- 751 Claeysman, M., Attié, J.-L., El Amraoui, L., Cariolle, D., Peuch, V.-H., Teyssèdre, H., Josse, B.,  
752 Ricaud, P., Massart, S., Piacentini, A., Cammas, J.-P., Livesey, N. J., Pumphrey, H. C., and  
753 Edwards, D. P.: A linear CO chemistry parameterization in chemistry-transport models:  
754 evaluation and application to data assimilation, *Atmos. Chem. Phys.*, 10, 6097-6115, 2010.
- 755 Claeysman, M., Attié, J.-L., Peuch, V.-H., El Amraoui, L., Lahoz, W. A., Josse, B., Ricaud, P., von  
756 Clarmann, T., Höpfner, M., Orphal, J., Flaud, J.-M., Edwards, D. P., Chance, K., Liu, X.,  
757 Pasternak, F., and Cantié, R.: A geostationary thermal infrared sensor to monitor the lowermost  
758 troposphere: O<sub>3</sub> and CO retrieval studies, *Atmos. Meas. Tech.*, 4, 297-317, 2011.
- 759 Clerbaux, C., Chazette, P., Hadji-Lazaro, J., Mégie, G., Müller, J.-F., and Clough, S. A.: Remote  
760 sensing of CO, CH<sub>4</sub>, and O<sub>3</sub> using a spaceborne nadir-viewing interferometer, *J. Geophys. Res.*,  
761 103, 18999–19013, doi:10.1029/98JD01422, 1998.
- 762 Courtier, P., Freyrier, C., Geleyn, J. F., Rabier, F., and Rochas, M.: The ARPEGE project at  
763 METEO-FRANCE. In: Proc ECMWF Workshop. Numerical methods in atmospheric modelling,  
764 9–13 Sept 1991, 2, 193–231. ECMWF, Shinfield Park, Reading, UK, 1991.
- 765 Crevoisier, C., Nobileau, D., Armante, R., Crépeau, L., Machida, T., Sawa, Y., Matsueda, H.,  
766 Schuck, T., Thonat, T., Pernin, J., Scott, N. A., and Chédin, A.: The 2007–2011 evolution of  
767 tropical methane in the mid-troposphere as seen from space by MetOp-A/IASI, *Atmos. Chem.*  
768 *Phys.*, 13, 4279-4289, doi:10.5194/acp-13-4279-2013, 2013.
- 769 Cros, B., Durand, P., and Cachier, H.: An overview of the ESCOMPTE campaign, *Atmos. Res.*,  
770 69(3-4), 241-279, 2004.
- 771 Dayan, U.: Climatology of Back Trajectories from Israel Based on Synoptic Analysis. *J. Climate*  
772 *Appl. Meteor.*, 25, 591–595. doi: [http://dx.doi.org/10.1175/1520-0450\(1986\)](http://dx.doi.org/10.1175/1520-0450(1986)), 1986.
- 773 Dentener, F., Stevenson, D., Cofala, J., Mechler, R., Amann, M., Bergamaschi, P., Raes, F., and  
774 Derwent, R.: The impact of air pollutant and methane emission controls on tropospheric ozone

- 775 and radiative forcing: CTM calculations for the period 1990–2030, *Atmos. Chem. Phys.*, 5,  
776 1731–1755, <http://www.atmos-chem-phys.net/5/1731/2005/>, 2005.
- 777 Drori, R., Dayan, U., Edwards, D. P., Emmons, L. K., and Erlick, C.: Attributing and quantifying  
778 carbon monoxide sources affecting the Eastern Mediterranean: a combined satellite, modelling,  
779 and synoptic analysis study, *Atmos. Chem. Phys.*, 12, 1067–1082, doi:10.5194/acp-12-1067-  
780 2012, 2012.
- 781 Dufour, A., Amodei, M., Ancellet, G., and Peuch, V.-H.: Observed and modelled “chemical  
782 weather” during ESCOMPTE, *Atmos. Res.*, 74, 161–189, 2005.
- 783 El Amraoui, L., Attié, J.-L., Semane, N., Claeysman, M., Peuch, V.-H., Warner, J., Ricaud, P.,  
784 Cammas, J.-P., Piacentini, A., Cariolle, D., Massart, S., and Bencherif, H.: Midlatitude  
785 stratosphere – troposphere exchange as diagnosed by MLS O<sub>3</sub> and MOPITT CO assimilated  
786 fields, *Atmos. Chem. Phys.*, 10, 2175–2194, 2010.
- 787 EUMETSAT, IASI Level 2 Products Guide, EUM/OPS-EPS/MAN/04/0033. Available on  
788 <http://oiswww.eumetsat.org/WEBOPS/eps-pg/IASI-L2/IASIL2-PG-0TOC.htm>, 2004.
- 789 Folberth, G. A., Hauglustaine, D. A., Lathière, J., and Brocheton, F.: Interactive chemistry in the  
790 Laboratoire de Météorologie Dynamique general circulation model: model description and  
791 impact analysis of biogenic hydrocarbons on tropospheric chemistry, *Atmos. Chem. Phys.*,  
792 6:2273–2319. [www.atmos-chem-phys.net/6/2273/2006/](http://www.atmos-chem-phys.net/6/2273/2006/), 2006.
- 793 Georgoulias, A. K., Kourtidis, K. A., Buchwitz, M., Schneising, O., and Burrows, J. P.: A case  
794 study on the application of SCIAMACHY satellite methane measurements for regional studies:  
795 the Greater Area of Eastern Mediterranean, *Int. J. Remote Sens.*, 32(3), 787–813,  
796 doi:10.1080/01431161.2010.517791, 2011.
- 797 Giorgi, F., and Lionello, P.: Climate change projections for the Mediterranean region, *Global and  
798 Planetary Change*, 63(2), 90–104, doi:10.1016/j.gloplacha.2007.09.005, 2008.
- 799 Hauglustaine, D. A., Hourdin, F., Jourdain, L., Filiberti, M.-A., Walters, S., Lamarque, J.-F., and  
800 Holland, E. A.: Interactive chemistry in the Laboratoire de Meteorologie Dynamique general

- 801 circulation model: description and background tropospheric chemistry evaluation, *J. Geophys.*  
802 *Res.*, 109:D04314. doi:10.1029/2003JD003957, 2004.
- 803 Hilton, F., Armante, R., August, T., Barnet, C., Bouchard, A., Camy-Peyret, C., Capelle, V.,  
804 Clarisse, L., Clerbaux, C., Coheur, P.-F., Collard, A., Crevoisier, C., Dufour, G., Edwards, D.,  
805 Faijan, F., Fourrié, N., Gambacorta, A., Goldberg, M., Guidard, V., Hurtmans, D., Illingworth,  
806 S., Jacquinet-Husson, N., Kerzenmacher, T., Klaes, D., Lavanant, L., Masiello, G., Matricardi,  
807 M., McNally, A., Newman, S., Pavelin, E., Payan, S., Péquignot, E., Peyridieu, S., Phulpin, T.,  
808 Remedios, J., Schlüssel, P., Serio, C., Strow, L., Stubenrauch, C., Taylor, J., Tobin, D., Wolf,  
809 W., and Zhou, D.: Hyperspectral Earth Observation from IASI: Five Years of Accomplishments,  
810 *B. Am. Meteor. Soc.*, 93, 347–370, doi:10.1175/BAMS-D-11-00027.1, 2012.
- 811 Hourdin, F., Musat, I., Bony, S., Braconnot, P., Codron, F., Dufresne, J.-L., Fairhead, L., Filiberti,  
812 M.-A., Friedlingstein, P., Grandpeix, J.-Y., Krinner, G., LeVan, P., Li, Z.-X., and Lott, F.: The  
813 LMDZ4 general circulation model: climate performance and sensitivity to parametrized physics  
814 with emphasis on tropical convection, *Clim. Dyn.*, 27, 787–813, doi:10.1007/s00382-006-0158-  
815 0, 2006.
- 816 Huszar, P., Teyssèdre, H., Cariolle, D., Olivié, D. J. L., Michou, M., Saint-Martin, D., Senesi, S.,  
817 Voldoire, A., Salas y Melia, D., Alias, A., Karcher, F., Ricaud, P., and Halenka, T.: Modeling  
818 the present and future impact of aviation on climate: an AOGCM approach with online coupled  
819 chemistry, *Atmos. Chem. Phys.*, 13, 10027-10048, doi:10.5194/acp-13-10027-2013, 2013.
- 820 Im, U. and Kanakidou, M.: Impacts of East Mediterranean megacity emissions on air quality,  
821 *Atmos. Chem. Phys.*, 12, 6335-6355, doi:10.5194/acp-12-6335-2012, 2012.
- 822 Imasu, R., Saitoh, N., and Niwa, Y.: Retrieval performance of GOSAT thermal infrared FTS sensor  
823 for measuring CO<sub>2</sub> concentrations, *Proc. SPIE 6744, Sensors, Systems, and Next-Generation*  
824 *Satellites XI*, 67440F, <http://dx.doi.org/10.1117/12.737796>, 2007.

- 825 IPCC: Climate change 2007: The physical science basis. Contribution of working group I to the  
826 fourth assessment report of the intergovernmental panel on climate change, Cambridge, UK and  
827 New York, USA, Cambridge University Press, 996 pp., 2007.
- 828 Josse, B., Simon, P., and Peuch, V.-H.: Rn-222 global simulations with the multiscale CTM  
829 MOCAGE, *Tellus*, 56B, 339–356, 2004.
- 830 Kallos, G., Astitha, M., Katsafados, P., and Spyrou, C.: Long-Range Transport of  
831 Anthropogenically and Naturally Produced Particulate Matter in the Mediterranean and North  
832 Atlantic: Current State of Knowledge, *J. Appl. Meteorol. Clim.*, 46, 1230-1251, 2007.
- 833 Kanakidou, M., Mihalopoulos, N., Kindap, T., Im, U., Vrekoussis, M., Gerasopoulos, E.,  
834 Dermitzaki, E., Unal, A., Kocak, M., Markakis, K., Melas, D., Kouvarakis, G., Youssef, A. F.,  
835 Richter, A., Hatzianastassiou, N., Hilboll, A., Ebojie, F., von Savigny, C., Ladstaetter-  
836 Weissenmayer, A., Burrows, J., and Moubasher, H.: Megacities as hot spots of air pollution in  
837 the East Mediterranean, *Atmos. Environ.*, 45, 1223–1235, 2011.
- 838 Krinner, G., Viovy, N., de Noblet-Ducoudré, N., Ogée, J., Polcher, J., Friedlingstein, P., Ciais, P.,  
839 Sitch, S., and Prentice, I. C.: A dynamic global vegetation model for studies of the coupled  
840 atmosphere-biosphere system, *Global Biogeochem. Cycles*, 19, GB1015,  
841 doi:10.1029/2003GB002199, 2005.
- 842 Kuze, A., Suto, H., Nakajima, M., and Hamazaki, T.: Thermal and near infrared sensor for carbon  
843 observation Fourier-transform spectrometer on the Greenhouse Gases Observing Satellite for  
844 greenhouse gases monitoring, *Appl. Opt.*, 48, 6716-6733, 2009.
- 845 Ladstätter-Weißenmayer, A., Heland, J., Kormann, R., von Kuhlmann, R., Lawrence, M. G.,  
846 Meyer-Arnek, J., Richter, A., Wittrock, F., Ziereis, H., and Burrows, J.-P.: Transport and build-  
847 up of tropospheric trace gases during the MINOS campaign: comparison of GOME, in situ  
848 aircraft measurements and MATCH-MPIC-data, *Atmos. Chem. Phys.*, 3, 1887–1902, 2003.
- 849 Lamarque, J.-F., Kyle, G. P., Meinshausen, M., Riahi, K., Smith, S. J., van Vuuren, D. P., Conley,  
850 A. J., and Vitt, F.: Global and regional evolution of short-lived radiatively-active gases and

- 851 aerosols in the Representative Concentration Pathways, *Climatic Change*, 109:191–212 DOI  
852 10.1007/s10584-011-0155-0, 2011.
- 853 Lamarque, J.-F., Shindell, D. T., Josse, B., Young, P. J., Cionni, I., Eyring, V., Bergmann, D.,  
854 Cameron-Smith, P., Collins, W. J., Doherty, R., Dalsoren, S., Faluvegi, G., Folberth, G., Ghan,  
855 S. J., Horowitz, L. W., Lee, Y. H., MacKenzie, I. A., Nagashima, T., Naik, V., Plummer, D.,  
856 Righi, M., Rumbold, S. T., Schulz, M., Skeie, R. B., Stevenson, D. S., Strode, S., Sudo, K.,  
857 Szopa, S., Voulgarakis, A., and Zeng, G.: The Atmospheric Chemistry and Climate Model  
858 Intercomparison Project (ACCMIP): overview and description of models, simulations and  
859 climate diagnostics, *Geosci. Model Dev.*, 6, 179-206, 2013.
- 860 Lefèvre, F., Brasseur, G. P., Folkins, I., Smith, A. K., and Simon, P.: Chemistry of the 1991–1992  
861 stratospheric winter: Three-dimensional model simulations, *J. Geophys. Res.*, 99, 9183–8195,  
862 1994.
- 863 Lelieveld, J., Berresheim, H., Borrmann, S., Crutzen, P. J., Dentener, F. J., Fischer, H., Feichter, J.,  
864 Flatau, P. J., Heland, J., Holzinger, R., Kormann, R., Lawrence, M. G., Levin, Z., Markowicz,  
865 K. M., Mihalopoulos, N., Minikin, A., Ramanathan, V., de Reus, M., Roelofs, G. J., Scheeren,  
866 H. A., Sciare, J., Schlager, H., Schultz, M., Siegmund, P., Steil, B., Stephanou, E. G., Stier, P.,  
867 Traub, M., Warneke, C., Williams, J., and Ziereis, H.: Global Air Pollution Crossroads over the  
868 Mediterranean, *Science*, 298, 5594, 794-799, DOI: 10.1126/science.1075457, 2002.
- 869 Lionello, P. (Ed.): *The Climate of the Mediterranean Region: From the past to the future*. 592p,  
870 Elsevier, 2012.
- 871 Liu, J. J., Jones, D. B. A., Worden, J. R., Noone, D., Parrington, M., and Kar, J.: Analysis of the  
872 summertime buildup of tropospheric ozone abundances over the Middle East and North Africa  
873 as observed by the Tropospheric Emission Spectrometer instrument, *J. Geophys. Res.*, 114,  
874 D05304, doi:10.1029/2008JD010993, 2009.

- 875 Masson, O., Piga, D., Gurriaran, R., and D'Amico, D.: Impact of an exceptional Saharan dust  
876 outbreak in France: PM10 and artificial radionuclides concentrations in air and in dust deposit,  
877 *Atmos. Env.*, 44, 20, 2478–2486, <http://dx.doi.org/10.1016/j.atmosenv.2010.03.004>, 2010.
- 878 Michou, M., and Peuch, V.-H.: Surface exchanges in the MOCAGE multiscale Chemistry and  
879 Transport Model, *J. Water Sci.*, 15, 173–203, 2002.
- 880 Michou, M., Saint-Martin, D., Teyssèdre, H., Alias, A., Karcher, F., Olivié, D., Voldoire, A., Josse,  
881 B., Peuch, V.-H., Clark, H., Lee, J. N., and Cheroux, F.: A new version of the CNRM  
882 Chemistry-Climate Model, CNRM-CCM: description and improvements from the CCMVal-2  
883 simulations, *Geosci. Model Dev.*, 4, 873–900, doi:10.5194/gmd-4-873-2011, 2011.
- 884 Millán, M. M., Salvador, R., Mantilla, E., and Kallos, G.: Photooxidant dynamics in the  
885 Mediterranean basin in summer: Results from European research projects, *J. Geophys. Res.*, 102,  
886 8811–8823, doi:10.1029/96JD03610, 1997.
- 887 Nabat, P., Solmon, F., Mallet, M., Kok, J. F., and Somot, S.: Dust emission size distribution impact  
888 on aerosol budget and radiative forcing over the Mediterranean region: a regional climate model  
889 approach, *Atmos. Chem. Phys.*, 12, 10545-10567, 2012.
- 890 Naik, V., Voulgarakis, A., Fiore, A. M., Horowitz, L. W., Lamarque, J.-F., Lin, M., Prather, M. J.,  
891 Young, P. J., Bergmann, D., Cameron-Smith, P. J., Cionni, I., Collins, W. J., Dalsøren, S. B.,  
892 Doherty, R., Eyring, V., Faluvegi, G., Folberth, G. A., Josse, B., Lee, Y. H., MacKenzie, I. A.,  
893 Nagashima, T., van Noije, T. P. C., Plummer, D. A., Righi, M., Rumbold, S. T., Skeie, R.,  
894 Shindell, D. T., Stevenson, D. S., Strode, S., Sudo, K., Szopa, S., and Zeng, G.: Preindustrial to  
895 present-day changes in tropospheric hydroxyl radical and methane lifetime from the  
896 Atmospheric Chemistry and Climate Model Intercomparison Project (ACCMIP), *Atmos. Chem.*  
897 *Phys.*, 13, 5277-5298, doi:10.5194/acp-13-5277-2013, 2013.
- 898 Park, M., Randel, W. J., Emmons, L. K., and Livesey, N. J.: Transport pathways of carbon  
899 monoxide in the Asian summer monsoon diagnosed from Model of Ozone and Related Tracers  
900 (MOZART), *J. Geophys. Res.*, 114, D08303, doi:10.1029/2008JD010621, 2009.



- 901 Peuch, V.-H., Amodei, M., Barthet, T., Cathala, M.-L., Josse, B., Michou, M., and Simon, P. :  
902 MOCAGE: Modèle de Chimie, Atmosphérique A Grande Echelle, Actes des Atelier de  
903 Modélisation de l'Atmosphère, Météo-France, 33–36, 1999.
- 904 Pfister, G., Petron, G., Emmons, L. K., Gille, J. C., Edwards, D. P., Lamarque, J.-F., J.-L. Attié, C.  
905 Granier, and Novelli, P. C: Evaluation of CO simulations and the analysis of the CO budget for  
906 Europe, *J. Geophys. Res.-Atmos.* (1984–2012), 109(D19), 2004.
- 907 Randel, W. J., and Park, M.: Deep convective influence on the Asian summer monsoon anticyclone  
908 and associated tracer variability observed with Atmospheric Infrared Sounder (AIRS), *J.*  
909 *Geophys. Res.*, 111, D12314, doi:10.1029/2005JD006490, 2006.
- 910 Razavi, A., Clerbaux, C., Wespes, C., Clarisse, L., Hurtmans, D., Payan, S., Camy-Peyret, C., and  
911 Coheur, P. F.: Characterization of methane retrievals from the IASI space-borne sounder, *Atmos.*  
912 *Chem. Phys.*, 9, 7889–7899, 2009.
- 913 Ricaud, P., Attié, J.-L., Teyssèdre, H., El Amraoui, L., Peuch, V.-H., Matricardi, M., and  
914 Schluessel, P.: Equatorial total column of nitrous oxide as measured by IASI on MetOp-A:  
915 implications for transport processes, *Atmos. Chem. Phys.*, 9, 3947-3956, doi:10.5194/acp-9-  
916 3947-2009, 2009.
- 917 Ricaud, P.: Variabilités de la vapeur d'eau et de la température troposphérique mesurées par le  
918 radiomètre micro-onde HAMSTRAD au Dôme C, Antarctique. Partie II : Résultats scientifiques,  
919 *La Météorologie*, 85, 35-46, doi: 10.4267/2042/53749, 2014.
- 920 Rodgers, C. D., *Inverse Methods for Atmospheric Sounding: Theory and Practice*, 1st ed.  
921 Singapore: World Scientific, 2000.
- 922 Rodwell, M. J., and Hoskins, B. J.: Monsoons and the dynamics of deserts, *Q. J. R. Meteorol. Soc.*,  
923 122, 1385-1404, 1996.
- 924 Saitoh, N., Touno, M., Hayashida, S., Imasu, R., Shiomi, K., Yokota, T., Yoshida, Y., Machida, T.,  
925 Matsueda, H., and Sawa, Y.: Comparisons between XCH<sub>4</sub> from GOSAT Shortwave and Thermal

- 926 Infrared Spectra and Aircraft CH<sub>4</sub> Measurements over Guam, SOLA, 8, 145–149,  
927 doi:10.2151/sola.2012-036, 2012.
- 928 Scheeren, H. A., Lelieveld, J., Roelofs, G. J., Williams, J., Fischer, H., de Reus, M., de Gouw, J. A.,  
929 Bolder, M., van der Veen, C., and Lawrence, M.: The impact of monsoon outflow from India  
930 and Southeast Asia in the upper troposphere over the eastern Mediterranean, Atmos. Chem.  
931 Phys., 3, 1589–1608, 2003.
- 932 Schicker, I., Radanovics, S., and Seibert, P.: Origin and transport of Mediterranean moisture and  
933 air, Atmos. Chem. Phys., 10, 5089–5105, doi:10.5194/acp-10-5089-2010, 2010.
- 934 Scheeren, H. A., Lelieveld, J., Roelofs, G. J., Williams, J., Fischer, H., de Reus, M., de Gouw, J. A.,  
935 Warneke, C., Holzinger, R., Schlager, H., Klüpfel, T., Bolder, M., van der Veen, C., and  
936 Lawrence, M.: The impact of monsoon outflow from India and Southeast Asia in the upper  
937 troposphere over the eastern Mediterranean, Atmos. Chem. Phys., 3, 1589–1608,  
938 doi:10.5194/acp-3-1589-2003, 2003.
- 939 Schlüssel, P., Hultberg, T. H., Phillips, P. L., August, T., and Calbet, X.: The operational IASI  
940 Level 2 Processor, Adv. Space Res., 36, 982–988, 2005.
- 941 Stockwell, W. R., Kirchner, F., Kuhn, M., and Seefeld, S.: A new mechanism for regional  
942 atmospheric chemistry modelling, J. Geophys. Res.: Atmospheres (1984–2012), 102(D22),  
943 25847–25879, 1997.
- 944 Susskind, J., Blaisdell, J. M., Iredell, L. and Keita, F.: Improved Temperature Sounding and Quality  
945 Control Methodology Using AIRS/AMSU Data: The AIRS Science Team Version 5 Retrieval  
946 Algorithm, IEEE Trans. Geosc. Remote Sens., 49, 883–907, 2011.
- 947 Szopa, S., Balkanski, Y., Schulz, M., Bekki, S., Cugnet, D., Fortems-Cheiney, A., Turquety, S.,  
948 Cozic, A., Déandreis, C., Hauglustaine, D., Idelkadi, A., Lathièrè, J., Lefèvre, F., Marchand, M.,  
949 Vuolo, R., Yan, N., and Dufresne, J.-L.: Aerosol and ozone changes as forcing for climate  
950 evolution between 1850 and 2100, Clim. Dynam., 40, 2223–2250, 2013. DOI:10.1007/s00382-  
951 012-1408-y

- 952 Turquety, S., Hadji-Lazaro, J., Clerbaux, C., Hauglustaine, D. A., Clough, S. A., Cassé, V.,  
953 Schlüssel, P., and Mégie, G.: Operational trace gas retrieval algorithm for the Infrared  
954 Atmospheric Sounding Interferometer, *J. Geophys. Res.*, 109, D21301,  
955 doi:10.1029/2004JD004821, 2004.
- 956 van der Werf, G. R., Randerson, J. T., Collatz, G. J., and Giglio, L.: Carbon emissions from fires in  
957 tropical and subtropical ecosystems, *Global Change Biol.*, 9, 547–562, 2003.
- 958 Voldoire, A., Sanchez-Gomez, E., Salas y Melia, D., Decharme, B., Cassou, C., Sénési, S., Valcke,  
959 S., Beau, I., Alias, A., Chevallier, M., Deque, M., Deshayes, J., Douville, H., Fernandez, E.,  
960 Madec, G., Maisonnave, E., Moine, M.-P., Planton, S., Saint-Martin, D., Szopa, S., Tyteca, S.,  
961 Alkama, R., Belamari, S., Braun, A., Coquart, L., and Chauvin, F.: The CNRM-CM5.1 global  
962 climate model: description and basic evaluation, *Clim. Dynam.*, doi:10.1007/s00382-011-1259-  
963 y, 2012.
- 964 Voulgarakis, A., Naik, V., Lamarque, J.-F., Shindell, D. T., Young, P. J., Prather, M. J., Wild, O.,  
965 Field, R. D., Bergmann, D., Cameron-Smith, P., Cionni, I., Collins, W. J., Dalsøren, S. B.,  
966 Doherty, R. M., Eyring, V., Faluvegi, G., Folberth, G. A., Horowitz, L. W., Josse, B.,  
967 MacKenzie, I. A., Nagashima, T., Plummer, D. A., Righi, M., Rumbold, S. T., Stevenson, D. S.,  
968 Strode, S. A., Sudo, K., Szopa, S., and Zeng, G.: Analysis of present day and future OH and  
969 methane lifetime in the ACCMIP simulations, *Atmos. Chem. Phys.*, 13, 2563-2587,  
970 doi:10.5194/acp-13-2563-2013, 2013.
- 971 Wanger, A., Peleg, M., Sharf, G., Mahrer, Y., Dayan, U., Kallos, G., Kotroni, V., Lagouvardos, K.,  
972 Varinou, M., Papadopoulos, A., and Luria, M.: Some Observational and Modelling Evidence of  
973 Long Range Transport of Air Pollutants from Europe Towards the Israeli Coast, *J. Geophys.*  
974 *Res.*, 105, 7177-7186, 2000.
- 975 Worden, J., Kulawik, S., Frankenberg, C., Payne, V., Bowman, K., Cady-Peirara, K., Wecht, K.,  
976 Lee, J. E., and Noone, D.: Profiles of CH<sub>4</sub>, HDO, H<sub>2</sub>O, and N<sub>2</sub>O with improved lower

- 977 tropospheric vertical resolution from Aura TES radiances, *Atmos. Meas. Tech.*, 5, 397–411,  
978 [www.atmos-meas-tech.net/5/397/2012/doi:10.5194/amt-5-397-2012](http://www.atmos-meas-tech.net/5/397/2012/doi:10.5194/amt-5-397-2012), 2012.
- 979 Wunch, D., Toon, G. C., Wennberg, P. O., Wofsy, S. C., Stephens, B. B., Fischer, M. L., Uchino,  
980 O., Abshire, J. B., Bernath, P., Biraud, S. C., Blavier, J.-F. L., Boone, C., Bowman, K. P.,  
981 Browell, E. V., Campos, T., Connor, B. J., Daube, B. C., Deutscher, N. M., Diao, M., Elkins, J.  
982 W., Gerbig, C., Gottlieb, E., Griffith, D. W. T., Hurst, D. F., Jiménez, R., Keppel-Aleks, G.,  
983 Kort, E. A., Macatangay, R., Machida, T., Matsueda, H., Moore, F., Morino, I., Park, S.,  
984 Robinson, J., Roehl, C. M., Sawa, Y., Sherlock, V., Sweeney, C., Tanaka, T., and Zondlo, M. A.:  
985 Calibration of the Total Carbon Column Observing Network using aircraft profile data, *Atmos.*  
986 *Meas. Tech.*, 3, 1351-1362, doi:10.5194/amt-3-1351-2010, 2010.
- 987 Xiong, X., Barnett, C., Maddy, E., Sweeney, C., Liu, X., Zhou, L., and Goldberg, M.:  
988 Characterization and validation of methane products from the Atmospheric Infrared Sounder  
989 (AIRS), *J. Geophys. Res.*, 113, G00A01, doi:10.1029/2007JG000500., 2008.
- 990 Yokota, T., Yoshida, Y., Eguchi, N., Ota, Y., Tanaka, T., Watanabe, H., and Maksyutov, S.: Global  
991 Concentrations of CO<sub>2</sub> and CH<sub>4</sub> Retrieved from GOSAT: First Preliminary Results, *SOLA*, 5,  
992 160-163, doi:10.2151/sola.2009, 2009.
- 993 Yoshida, Y., Kikuchi, N., Morino, I., Uchino, O., Oshchepkov, S., Bril, A., Saeki, T., Schutgens,  
994 N., Toon, G. C., Wunch, D., Roehl, C. M., Wennberg, P. O., Griffith, D. W. T., Deutscher, N.  
995 M., Warneke, T., Notholt, J., Robinson, J., Sherlock, V., Connor, B., Rettinger, M., Sussmann,  
996 R., Ahonen, P., Heikkinen, P., Kyrö, E., Mendonca, J., Strong, K., Hase, F., Dohe, S., and  
997 Yokota, T.: Improvement of the retrieval algorithm for GOSAT SWIR XCO<sub>2</sub> and XCH<sub>4</sub> and  
998 their validation using TCCON data, *Atmos. Meas. Tech.*, 6, 1533-1547, doi:10.5194/amt-6-  
999 1533-2013, 2013.
- 1000 Ziv, B., Saaroni, H., and Alpert, P.: The factors governing the summer regime of the eastern  
1001 Mediterranean, *Int. J. Climatol.*, 24, 1859–1871, doi: 10.1002/joc.1113, 2004.
- 1002

1002 **Table 1.** Nadir-viewing instruments having the capabilities to measure CH<sub>4</sub> in the troposphere.

1003 Please, refer to the text for the acronyms.

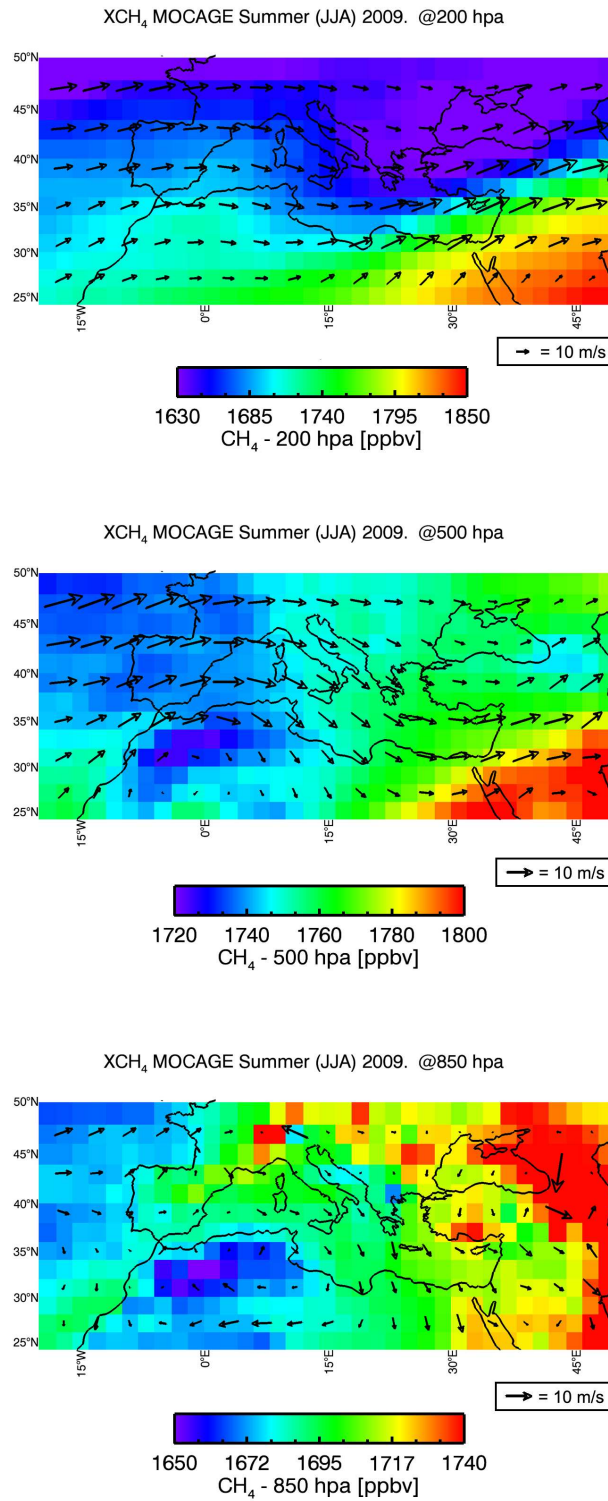
1004

<b>Platform</b>	<b>Instrument</b>	<b>Operation time</b>	<b>Wavelength</b>	<b>References</b>
ADEOS-1	IMG	1996-1997	TIR	Clerbaux et al. (1998)
ENVISAT	SCIAMACHY	2002-2012	NIR	Buchwitz et al. (2000)
Aura	TES	2004-date	TIR	Worden et al. (2012)
GOSAT	TANSO-FTS	2008-date	SWIR & TIR	Yokoto et al. (2009)
Aqua	AIRS	2004-date	TIR	Xiong et al. (2008)
MetOp-A	IASI	2008-date	TIR	Hilton et al. (2012)
MetOp-B	IASI	2012-date	TIR	
MetOp-C	IASI	Expected in 2016	TIR	

1005

1006

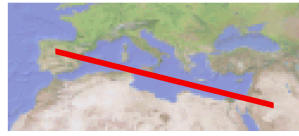
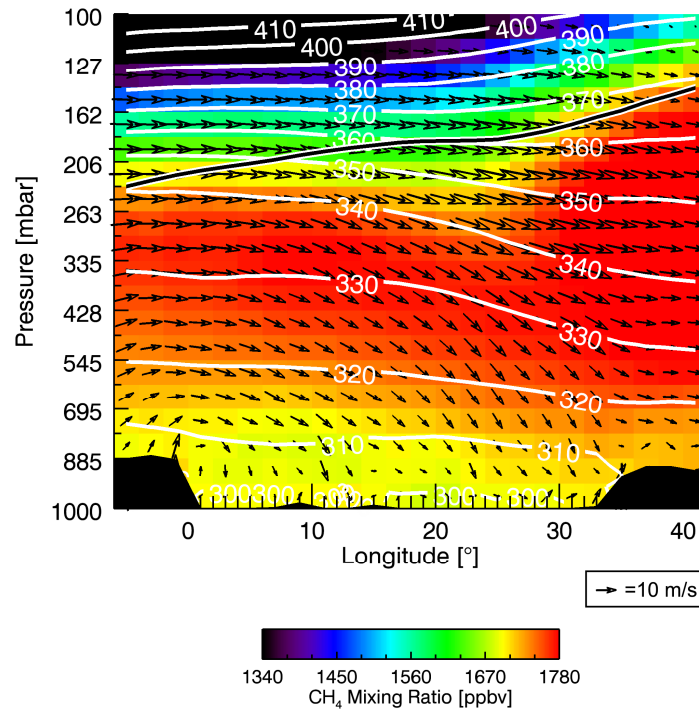
1007



1007

1008 **Figure 1.** (From bottom to top) Fields of CH<sub>4</sub> as calculated by MOCAGE and averaged for summer  
 1009 (JJA) 2009 at 850, 500 and 200 hPa. Superimposed are the horizontal winds from ARPEGE  
 1010 averaged over the same period. In order to highlight the CH<sub>4</sub> horizontal gradients, the range of the  
 1011 colour scale changes from top to bottom.

1012

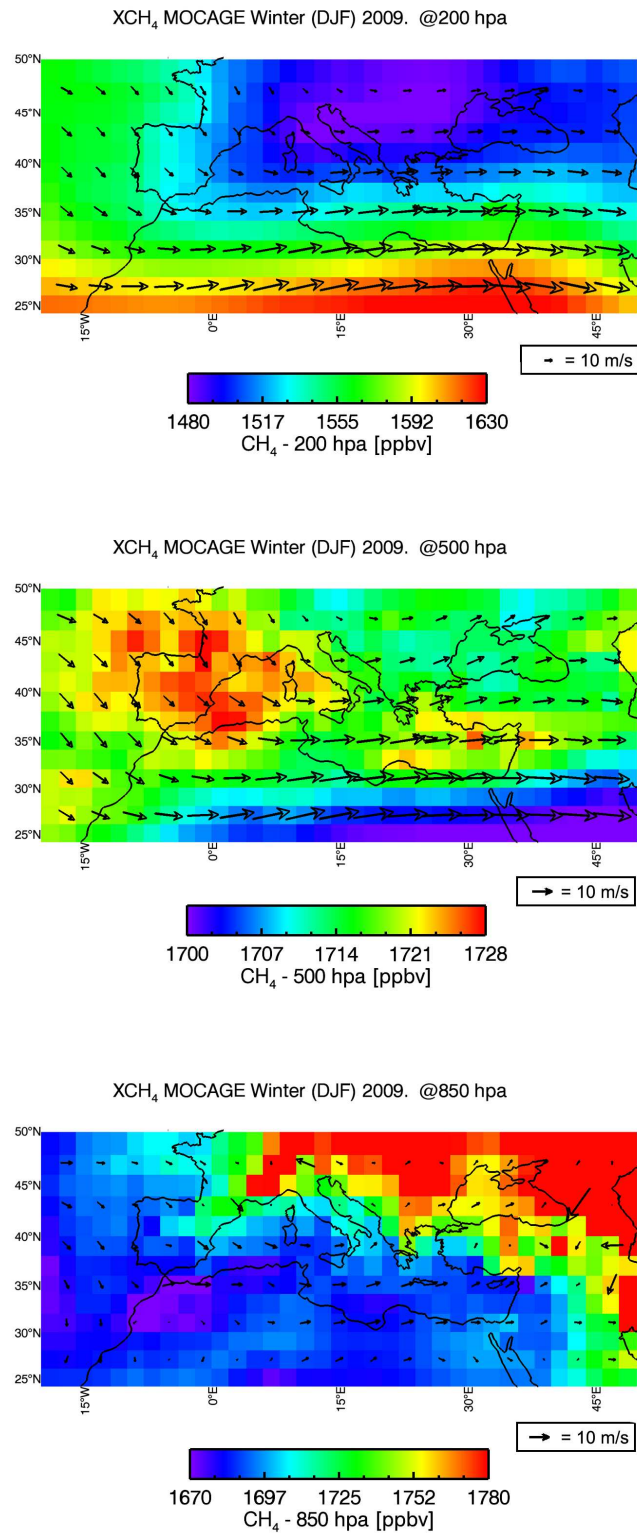
MOCAGE summer (JJA) 2009. CH<sub>4</sub> [ppbv]

1013

1014 **Figure 2.** Vertical distribution of CH<sub>4</sub> as calculated by MOCAGE and averaged for JJA 2009 as a  
 1015 function of longitude along the red line represented above the Figure. Superimposed are the  
 1016 associated longitudinal and vertical winds from ARPEGE, together with the isentropes (white lines)  
 1017 and the cold point tropopause from NCEP/NCAR reanalyses (black line) averaged over the same  
 1018 period.

1019

1020



1020

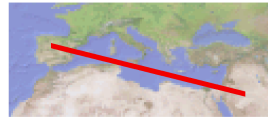
1021 **Figure 3.** Same as Fig. 1, but for winter (DJF) 2009.

1022

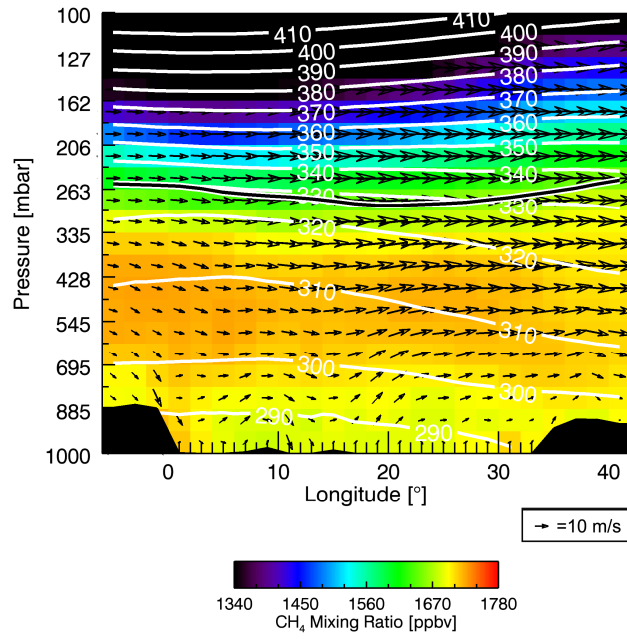
1023



1023



MOCAGE winter (DJF) 2009. CH<sub>4</sub> [ppbv]



1024

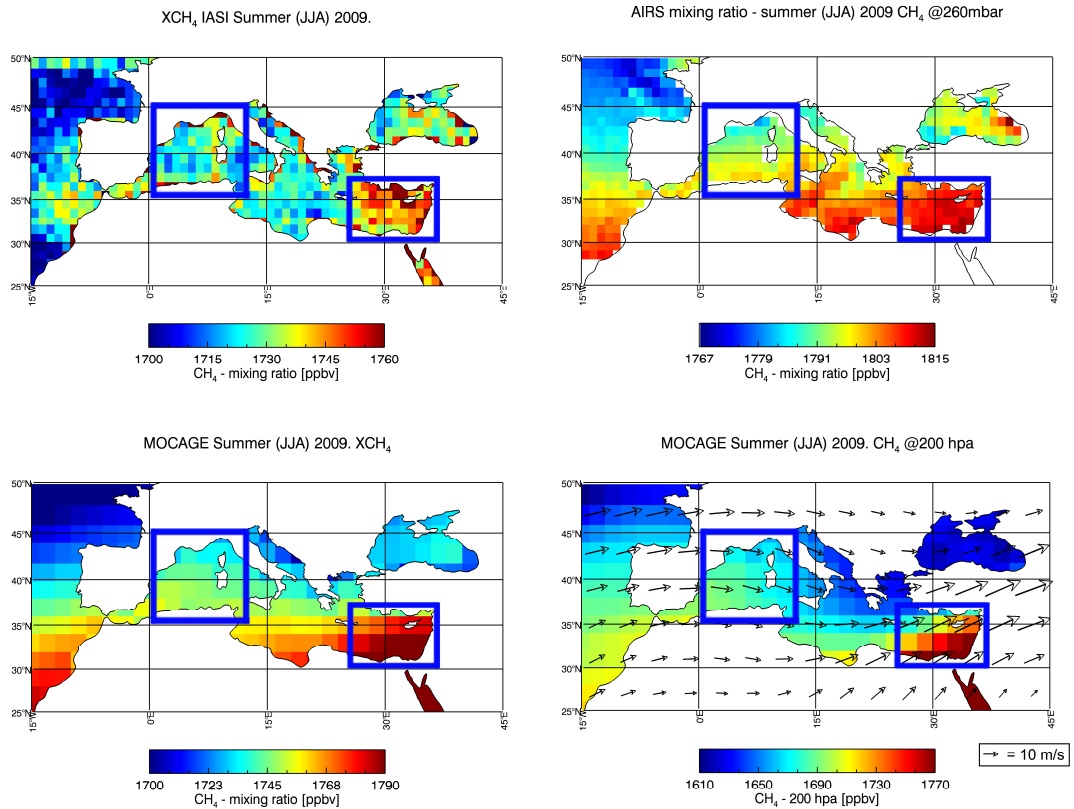
1025 **Figure 4.** Same as Fig. 2, but for winter (DJF) 2009.

1026

1027

1027

1028



1029

1030 **Figure 5.** Field of total columns of CH<sub>4</sub> as measured by IASI and averaged for summer (JJA) 2009

1031 (top left), and field of CH<sub>4</sub> at 260 hPa as measured by AIRS and averaged for JJA 2009 (top right).

1032 (Bottom) Same as above but as calculated by MOCAGE. Satellite data are represented in a 1°x1°

1033 resolution whilst model data are shown in a 2°x2° resolution. The two blue squares in the lower left

1034 Figure represent the Western and Eastern Mediterranean Basins where the measured and modelled

1035 data are selected over the Mediterranean Sea. Superimposed are the horizontal winds from

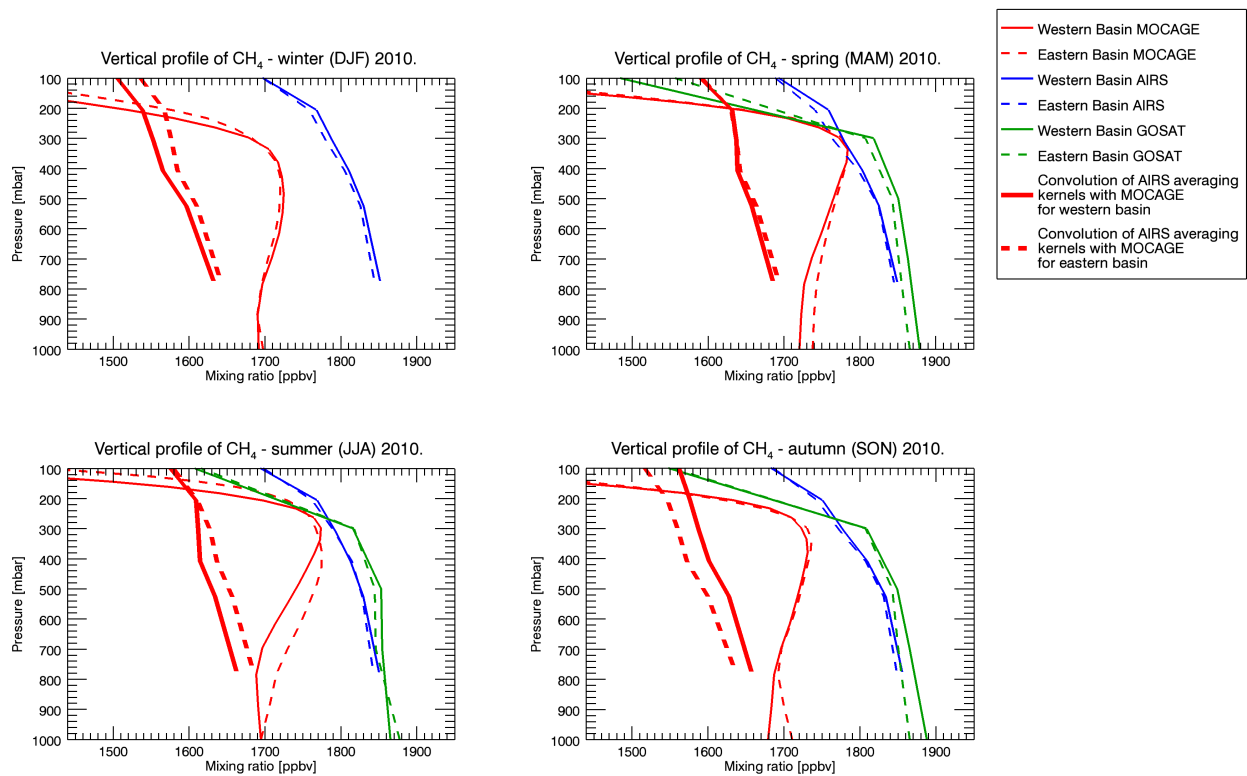
1036 ARPEGE at 200 hPa averaged over the same period (bottom right). In order to highlight the CH<sub>4</sub>

1037 horizontal gradients, the range of the colour scale changes for each figure.

1038

1039

1039



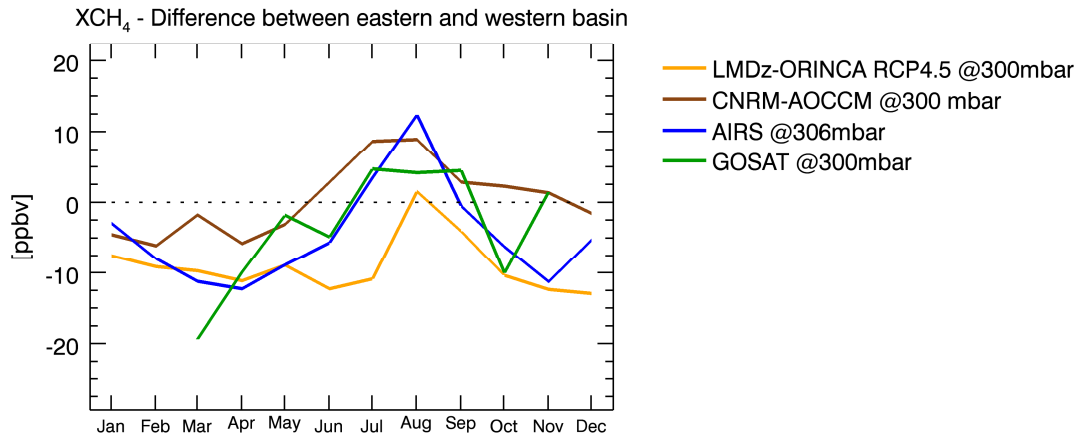
1040

1041 **Figure 6.** (From top to bottom and from left to right) Seasonally-averaged vertical profiles of CH<sub>4</sub>  
 1042 as measured by AIRS (blue lines) and GOSAT (green lines), and as calculated by MOCAGE (thin  
 1043 red lines) over the Eastern (dashed lines) and Western (solid lines) MBs in winter, summer, spring  
 1044 and autumn 2010. Also shown are the seasonally-averaged MOCAGE profiles convolved with the  
 1045 AIRS averaging kernels (thick red lines) for the four seasons over the Eastern (dashed lines) and  
 1046 Western (solid lines) MBs.

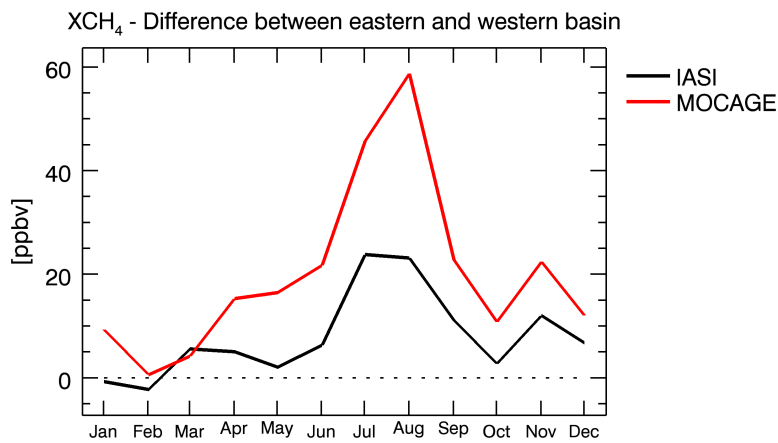
1047

1048

1048



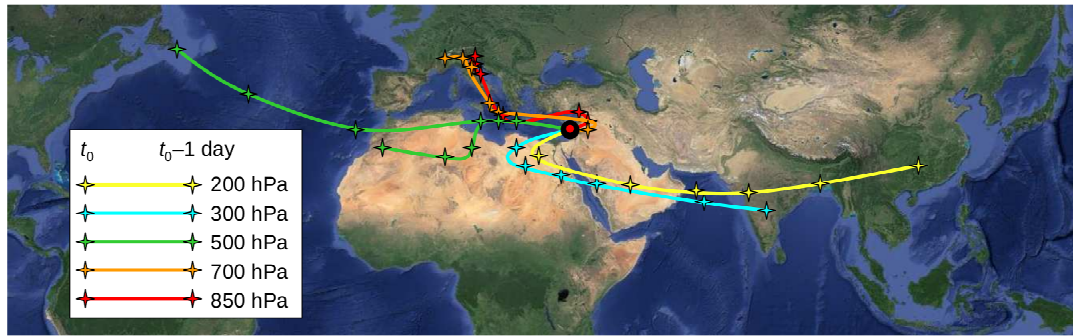
1049



1050

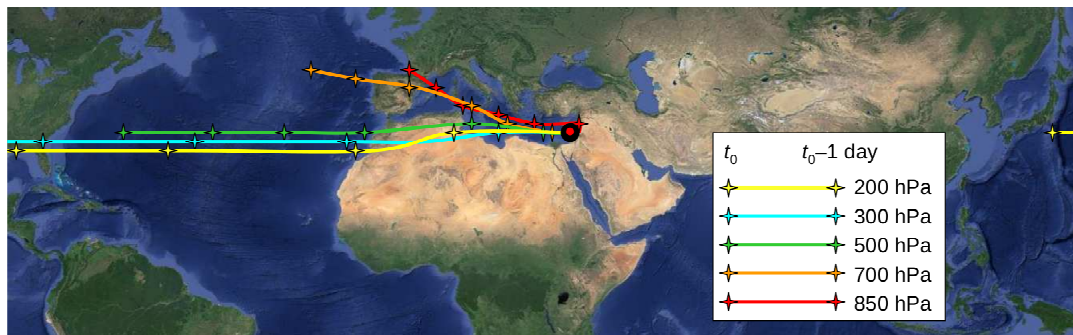
1051 **Figure 7.** (Top) Seasonal evolution of the difference in the CH<sub>4</sub> fields between the Eastern and  
 1052 Western MB as measured by AIRS (blue line) and GOSAT (green line) at 306 and 300 hPa,  
 1053 respectively and as calculated by LMDz-OR-INCA (yellow line) and CNRM-AOCCM (brown  
 1054 line). (Bottom) Seasonal evolution of the difference in the CH<sub>4</sub> total columns between the Eastern  
 1055 and Western MB as measured by IASI (black line) and as calculated by MOCAGE (red line). The  
 1056 LMDz-OR-INCA and CNRM-AOCCM data sets cover the climatological period 2001-2010. The  
 1057 MOCAGE and IASI data sets cover the period 2008-2011 whilst the satellite AIRS and GOSAT  
 1058 data sets are representative of the year 2010.

6-Day Backtrajectories from the Eastern Mediterranean Basin  
July-August 2001-2010



1059

6-Day Backtrajectories from the Eastern Mediterranean Basin  
January-February-March 2001-2010

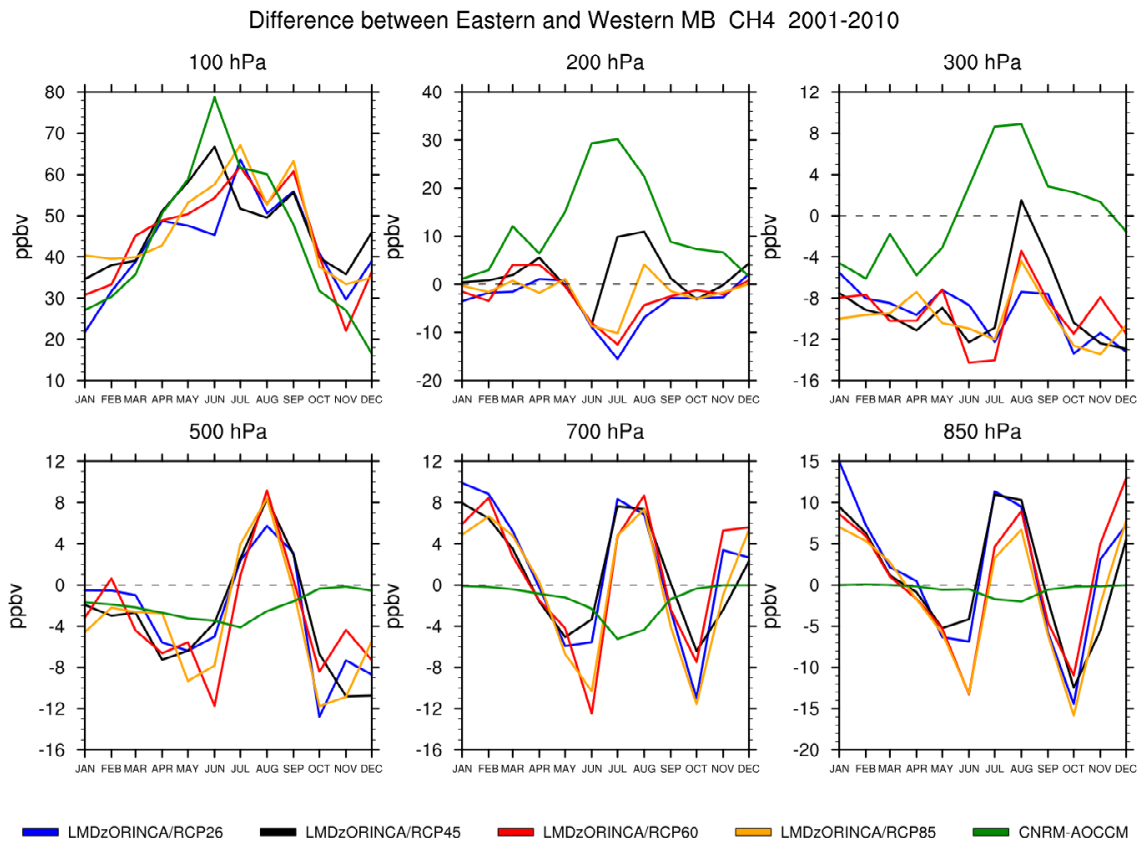


1060

1061 **Figure 8.** (Top) Climatological six-day back-trajectories from the point at  $33^{\circ}$  N,  $35^{\circ}$  E located in  
 1062 the Eastern Mediterranean Basin (red filled circle) calculated from the British Atmospheric Data  
 1063 Centre trajectory service (<http://badc.nerc.ac.uk/community/trajectory/>) from 1st July to 31st  
 1064 August from 2001 to 2010 every 12 hours at 850 (red line), 700 (orange line), 500 (green line), 300  
 1065 (blue line) and 200 hPa (yellow line). The position of the gravity center of each distribution at each  
 1066 level is represented every 24 hours by a star. (Bottom) Same as top, but calculated from 1<sup>st</sup> January  
 1067 to 31<sup>st</sup> March 2001-2010.

1068

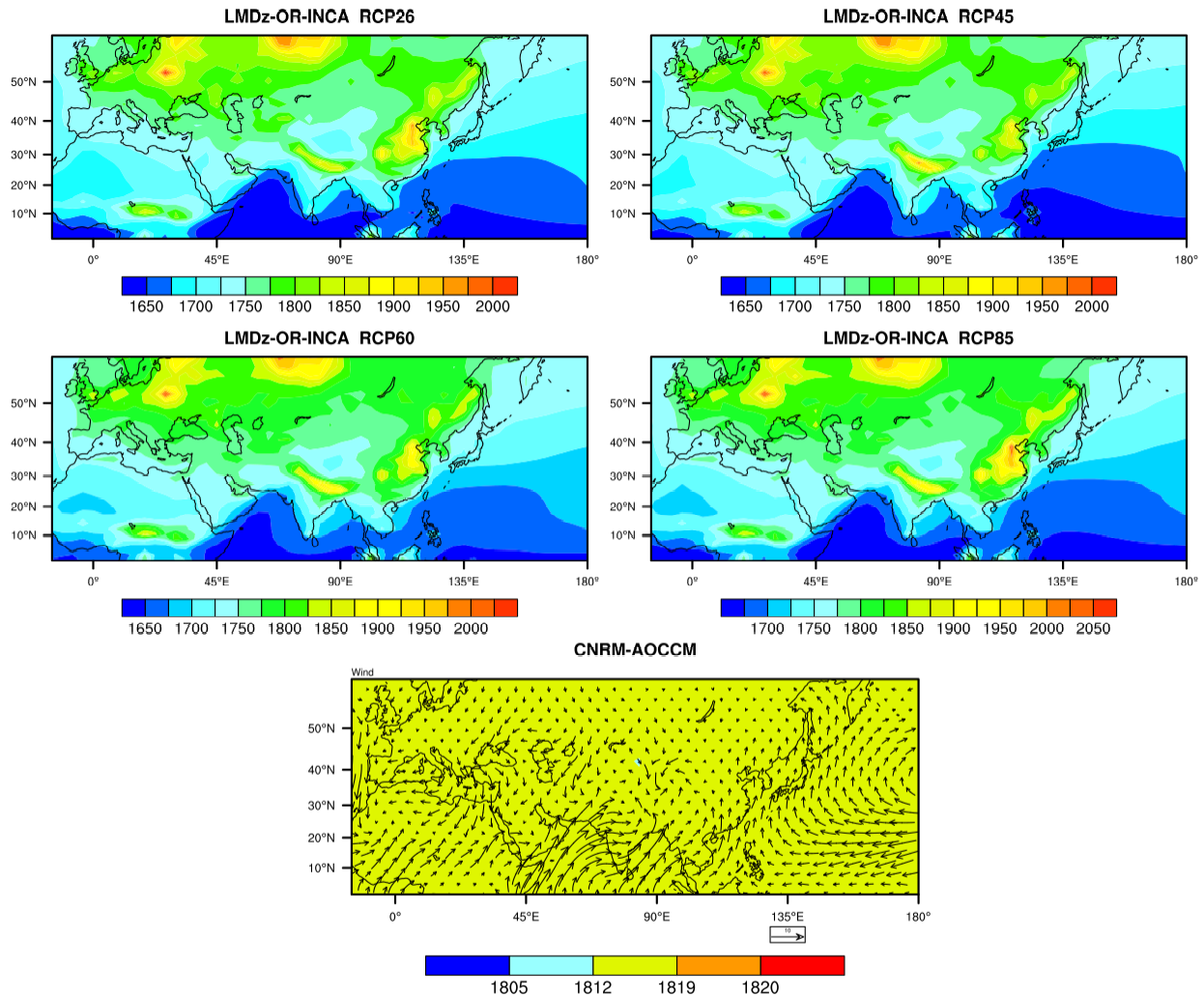
1068



1069

1070 **Figure 9.** (From top to bottom and from left to right) Seasonal evolution of the difference in the  
 1071 CH<sub>4</sub> fields between the Eastern and Western MB over the climatological period 2001-2010 at 100,  
 1072 200, 300, 500, 700 and 850 hPa as calculated by CNRM-AOCCM (green) model and LMDz-OR-  
 1073 INCA according to the 4 IPCC scenarios: RPCs 2.6 (blue), 4.5 (black), 6.0 (red) and 8.5 (yellow).  
 1074 See section 2.2 for more details.

1075

CH<sub>4</sub> (ppbv) surface level JJA 2001-2010

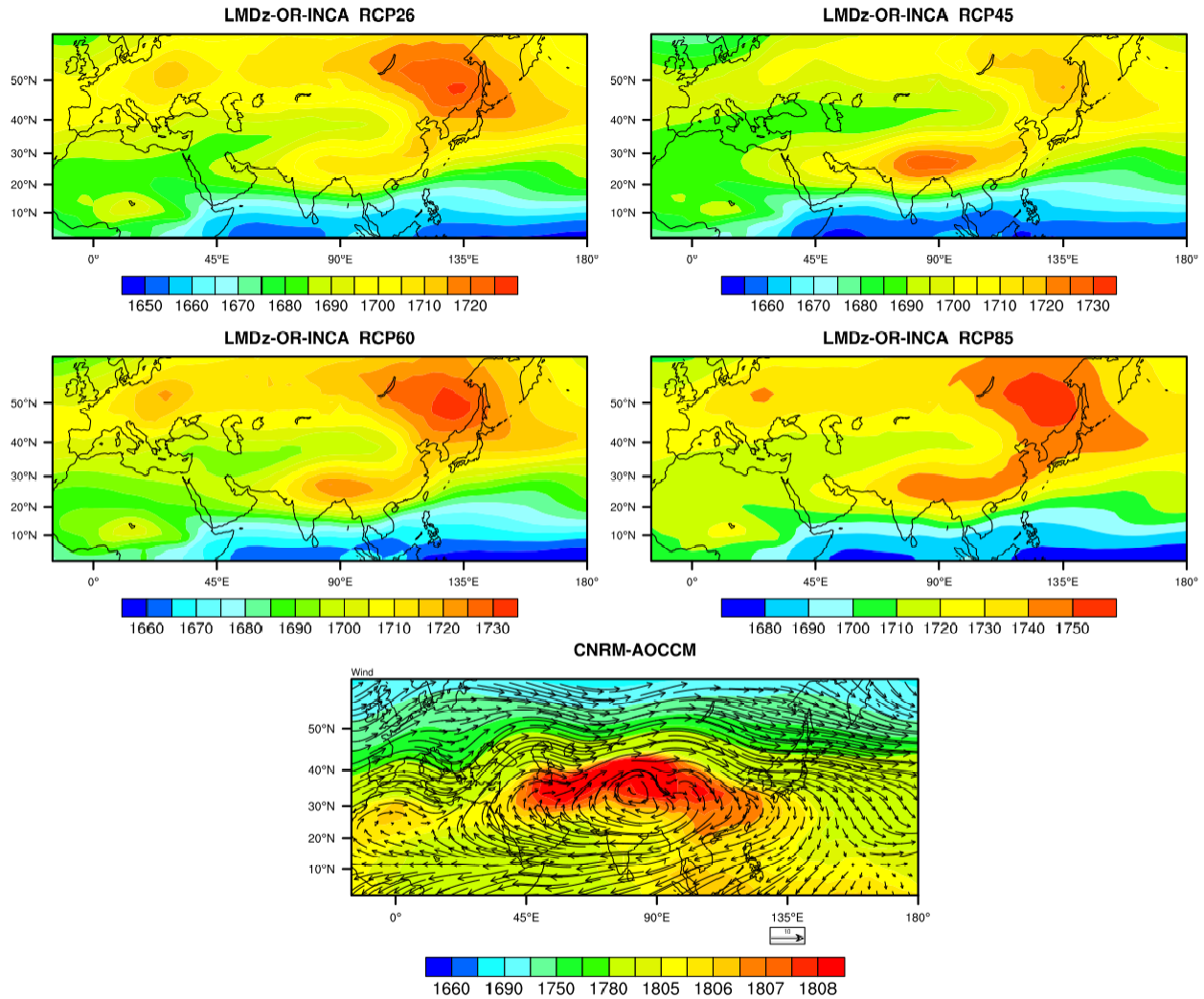
1076

1077 **Figure 10.** Fields of surface CH<sub>4</sub> as calculated by the CNRM-AOCCM model (bottom) and the  
 1078 LMDz-OR-INCA model (top and centre) according to the 4 IPCC scenarios (RCPs 2.6 (top left),  
 1079 4.5 (top right), 6.0 (centre left) and 8.5 (centre right)) averaged over the summer season (JJA) and  
 1080 the climatological period 2001-2010. Superimposed to the CNRM-AOCCM CH<sub>4</sub> fields (bottom) is  
 1081 the wind field at the surface averaged over the same period. Note that the range of the colour scale  
 1082 changes for each figure and that the surface CH<sub>4</sub> for CNRM-AOCCM (bottom) is constant.

1083

1084



CH<sub>4</sub> (ppbv) 200 hPa JJA 2001-2010

1084

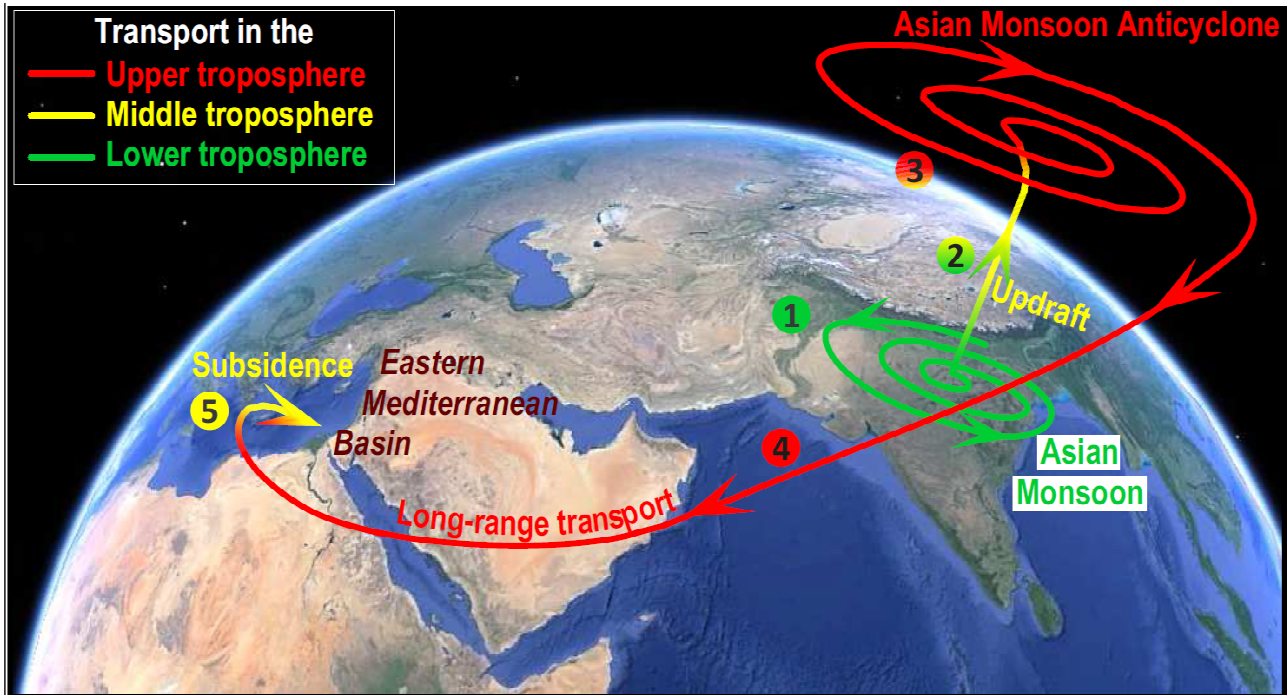
1085 **Figure 11.** Fields of CH<sub>4</sub> as calculated by the CNRM-AOCCM model (bottom) and the LMDz-OR-  
 1086 INCA model (top and centre) considering the 4 IPCC scenarios (RCPs 2.6 (top left), 4.5 (top right),  
 1087 6.0 (centre left) and 8.5 (centre right)) at 200 hPa averaged over the summer season (JJA) and the  
 1088 climatological period 2001-2010. Superimposed to the CNRM-AOCCM CH<sub>4</sub> fields (bottom) is the  
 1089 wind field at 200 hPa averaged over the same period. Note that the range of the colour scale  
 1090 changes for each figure and that the colour scale for the CNRM-AOCCM model (bottom) is non  
 1091 linear.

1092

1093



1093



1094

1095 **Figure 12.** Schematic representation of the processes impacting the mid-to-upper tropospheric  
 1096 pollutants, including CH<sub>4</sub>, above the Eastern Mediterranean Basin in summer (July-August). (1)  
 1097 Trapping of lower tropospheric pollutants in the Asian monsoon. (2) Updraft of pollutants in the  
 1098 Asian monsoon up to the upper troposphere. (3) Build-up of pollutants within the Asian monsoon in  
 1099 the upper troposphere. (4) Large-scale re-distribution of pollutants by the Asian Monsoon  
 1100 Anticyclone to the Middle East and North Africa in the upper troposphere. (5) Build-up of  
 1101 pollutants though descent down to the middle troposphere above the Eastern Mediterranean Basin.

1102